Tilt Pad Bearing Distributed Pad Inlet Temperature With Machine Learning—Part II: Morton Effect

Jongin Yang[1]
Mem. ASME
Department of Mechanical Engineering,
Texas A&M University,
College Station, TX 77840
e-mail: jiyang@tamu.edu

Alan Palazzolo
Fellow ASME
Department of Mechanical Engineering,
Texas A&M University,
College Station, TX 77840
e-mail: a-palazzolo@tamu.edu

The Morton effect (ME) occurs when a bearing journal experiences asymmetric heating due to synchronous vibration, resulting in thermal bowing of the shaft and increasing vibration. An accurate prediction of the journal's asymmetric temperature distribution is critical for reliable ME simulation. This distribution is strongly influenced by the film thermal boundary condition at the pad inlets. Part I utilizes machine learning (ML) to obtain a two-dimensional radial and axial distribution of temperatures over the leading-edge film cross section. The hybrid finite volume method (FVM)—bulk flow method of Part I eliminated film temperature discontinuities and is utilized in Part II for improving accuracy and efficiency of ME simulation. [DOI: 10.1115/1.4052172]

Keywords: journal bearings, thermoelastohydrodynamic lubrication

1 Introduction

The Morton effect (ME) occurs most frequently in high-performance, high-speed machines with rotors having large overhung masses, and supported by fluid-film bearings. The journal is forced to precess, or orbit, in a synchronous, elliptical motion by rotor mass imbalance forces, as shown in Fig. 1(*a*). The synchronous orbit exposes the same point on the journal to the maximum heat generation, and near minimum film thickness, each rotation of the shaft, as depicted in Fig. 1(*b*). This results in an asymmetric temperature change that varies sinusoidally around the circumference of the journal.

The maximum temperature (journal hot spot) lags slightly behind the minimum film thickness (journal high spot). Figure 1(*c*) illustrates the shaft thermal bow induced by the journal temperature asymmetry. Similar with imbalance, bow also drives synchronous vibration, which alters the journal orbit, journal heating, and shaft bow. This cycle forms a positive feedback loop under certain conditions resulting in a synchronous vibration instability, also known as, the ME.

Morton [1] and Hesseborn [2] first discovered the ME phenomena, and there has been expanding academic and industrial interest in the subject ever since [3,4]. It is noted that the ME needs to be distinguished from the Newkirk effect [5]. The latter has rub-induced asymmetric journal heating, and unlike ME, has coincident high and hot spots. The recent literature review [5] points out that the ME is still not fully understood in academic and industrial circles and is being intensely researched. In its most complete sense, the ME is a complex, transient, three-dimensional (3D), multiphysics phenomenon, demanding extensive computation time for simulation. Thus, much past research [7–12] was conducted with simplified models for ME instability prediction.

In 1993, Keogh and Morton [6] presented the first ME model, utilizing concepts from classic control theory to evaluate ME instability. Short bearing theory and a two-dimensional (2D) energy equation with constant viscosity were used for the fluid-film modeling. 2D energy equations were also used for modeling the journal and bearing heat transfer, and the journal surface temperature was estimated from perturbed and predefined orbits. The influence of time-varying orbit and shaft bending effects were investigated in their 1994 paper [7], along with coupled rotor-

bearing system dynamics. Gomiciaga and Keogh utilized computational fluid dynamics (CFD) for the prediction of journal differential heating in 1999 [8]. The journal temperature was solved at several predefined orbit points, and differential heating was evaluated from the orbit-averaging heat flux. Journal 3D heat conduction was included, but thermal bending and expansion were not considered.

Balbahadur and Kirk proposed a new ME instability prediction method based on an imbalance threshold criterion in 2004 [9,10]. ME instability was judged to occur when the resultant unbalance force exceeded 15% of the rotor weight. The fluid-film model assumed a linear velocity profile and used a one-dimensional (1D) circumferential temperature assumption. Thermal deflection was expressed as a function of a circumferential temperature difference (∆T), and the hot spot and high spot were assumed to be coincident. Murphy and Lorenz utilized linear model, phasor influence (sensitivity) coefficients among vibration, unbalance, and ∆T to predict ME instability in 2010 [11]. The relations were applied with classic eigenvalue analysis for ME instability evaluation. Energy equations for the fluid-film, shaft, and bearing were not explicitly treated, but were assumed to be solved by conventional non ME bearing codes, in this "fast" ME evaluation method. The angle between the high and hot spots was obtained from empirical sources. Childs and Saha calculated the journal temperature for a wide range of elliptical orbits, represented with forward and
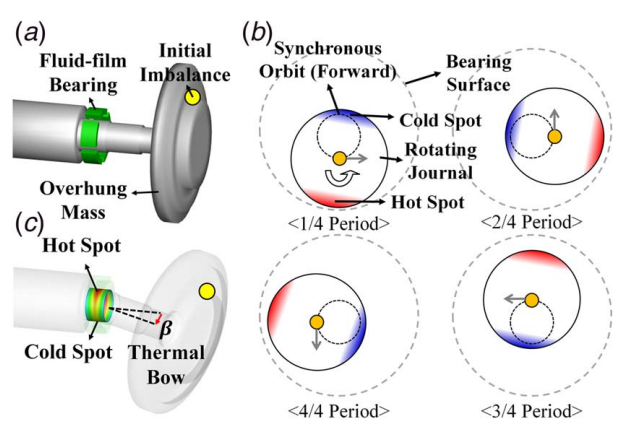
Fig. 1 ME cyclic asymmetric heating of a journal: (*a*) initial imbalance, (*b*) synchronous orbit at bearing, and (*c*) journal ∆*T* and thermal bow generation

---

backward whirl circular orbits, in 2012 [12]. Journal temperature ΔT associated with any specific orbit was then obtained via interpolating values in lookup tables, during an iterative evaluation of ME stability. Rotor bending was assumed to vary linearly with ΔT, and an equivalent thermally induced imbalance was assumed.

Efforts [13–17] to better understand and predict the ME have been undertaken with higher fidelity models and extensive computational load, in parallel with the more simplified, and intuitively based approaches [7–12]. These efforts use staggered nonlinear transient, numerical integration to enable solution, accounting for the very long thermal time constants and very short vibration time constants inherent with the ME [5]. The high fidelity modeling approaches have evolved to incrementally remove the dimensional, heating, flow, and vibration assumptions of the simplified, intuitive approaches.

Lee and Palazzolo used a 2D, finite element method (FEM)-based thermal hydrodynamic model, with transient analysis, for modeling the ME in 2013 [13]. A staggered integration scheme provided an efficient computational approach for the widely separated thermal and vibration time constant ME problem. Suh and Palazzolo extended the 2D model to a 3D model for the entire shaft, bearing, and fluid-film computational domains in 2014 [14,15]. A distributed thermal imbalance model replaced the previous approach of lumping the "thermally induced" unbalance at an overhung node. In 2016, Tong et al. [16] advanced Suh's work by replacing the thermally induced imbalance model with a more realistic thermal bow model, in the rotor-dynamic simulation. Their ME model was extended to include double overhung masses in Refs. [17,18].

The importance of accurate asymmetric journal temperature prediction cannot be overstated for accurate simulation of the ME, since this determines the thermal shaft bow that drives the ME vibration increase. Film temperatures have the greatest influence on journal temperature; therefore, the former must be evaluated very accurately in the radial, circumferential, and axial directions of the fluid film. Most recent approaches, i.e., Refs. [13–18] have adopted FEM for solving the Reynolds and energy equations in the fluid-film. The shortcoming of FEM is that the contravention of local energy conservation (temperature discontinuity) is observed near the journal surfaces, which can greatly influence heat flow into the journal.

Accurate simulation of TPJB requires complex multiphysics models as in Refs. [19–21] and as described in Part I. This need is especially important for simulating the Morton effect. References [22–25] very clearly demonstrated that bearing oil feed conditions may significantly affect hydrodynamic bearing performance. This confirms the importance of the thermal mixing modeling between pads, as stressed in Part I. The present work advances these findings to show that the conventional MC approach may be inadequate for providing accurate pad film inlet temperatures. Yang and Palazzolo [26] reported in 2020 that the uncertainty and approximation of the mixing coefficient MC approach for predicting uniform leading-edge film temperatures could introduce significant error in tilting pad journal bearing (TPJB) temperature and performance predictions. This work also demonstrated the significant impact that radial temperature and axial MC distributions, at the fluid-film leading-edge, could have on the journal temperatures. Yang and Palazzolo applied a CFD-based machine learning technique for obtaining more accurate MC, for TPJB dynamic coefficient prediction in 2020 [27,28]. The regression yielded a single area averaged MC, neglecting possible radial and axial dependence at the pad leading-edge.

Part I addressed the two weaknesses of conventional methods for predicting accurate journal temperature distributions, which is key for accurate ME prediction. These are film temperature discontinuities and radial and axial temperature variations at the pad leading-edge inlets. The finite volume method (FVM) was shown to produce continuous film temperature distributions satisfying local energy conservation. In addition, a direct solving procedure for the FVM was provided and demonstrated to significantly

accelerate computational speed. Moreover, the 2D temperature distribution at the fluid-film leading-edge was determined through a 3D hybrid between pad (HBP) model and implemented in a dynamic coefficient application by using a machine learning, axial mixing coefficient (MLAMC) approach. Here, the term "Between Pad" indicates the oil supply region (groove) between pads. The approach was validated against full model CFD solution for static responses and dynamic coefficient prediction.

The primary objective of Part II is to investigate the effects of implementing the modeling improvements demonstrated in Part I, to improving ME predictions. These improvements include continuous temperature distributions, radial and axially varying temperature at the pad inlets, and accelerated computational time. Fluid thermal inertia between pads, centrifugal force effect, pad flexibility, and supply oil flow effect are considered in the dynamic simulation. For validation, the proposed model is compared with experimental data [29], and the drawbacks of the FEM-based and conventional MC approaches are investigated for ME simulation.

Summarizing, the original contributions of Part II relative to the literature, including the author's prior work include:

(a) More accurate journal temperature prediction by accounting for radially and axially varying film temperatures at each pad inlet, utilizing the methods of Part I.
(b) Continuous updating of the axial mixing coefficients as the pad angles, journal position, and other variables change during the nonlinear, transient ME simulation.
(c) The use of a novel numerical algorithm to accelerate solution by the finite volume method enables the ME to be simulated with a reasonable computation time and load, for practical implementation by industry.
(d) Improved ME simulation accuracy is demonstrated by comparison with one of the very few ME test cases in the literature.
(e) Investigate the supply flowrate effect, through the axial mixing coefficients varying with supply flowrate, and the pad flexibility effect on the ME.

2 Morton Effect Simulation Modeling Methods

2.1 Overview. Figure 2 illustrates the constituent subdomains for ME simulation modeling. ME simulation requires more complex computational domains and a more intensive computational load than for static and dynamic coefficient prediction, as presented in Part I. The rotor-bearing system consists of the linear bearing, nonlinear bearing (TPJB), and rotor with the overhung mass, as shown in Fig. 2(a). Most ME theoretical models overlap with the model presented in Part I. A major difference is that the present model derives its thermal bow and imbalance distribution from a hybrid finite element method (HFEM) [16] dynamics model of the shaft. The HFEM includes a 3D solid element shaft in the journal region and a 1D beam domain elsewhere. A second major distinction is the use of inner between pad (IBP) and outer between pad (OBP) subdomains, which provide a significantly more accurate representation of the 3D mixing effect between pads, through coupling with the MLAMC.

The computational domains use suitable numerical methods for efficient time-cost and accuracy solutions. The governing equations in the fluid-type domain are discretized by the FVM to follow the conservation rules strictly, and the FEM is utilized for the solid-type domains. Table 1 summarizes the theories, dimensions, numerical methods, and dependent variables of each computational domain.

Numerical time integration is carried out for the dynamic and thermal models of all domains. The heat capacities of the solid domains are substantially higher than the fluid domains. Thus, the temperature changes in the solid domains have a much larger time constant than that of the fluid-film domains, and of the high frequency vibrations. Thus, a staggered time integration scheme [13] is applied for an efficient and accurate numerical solution of the coupled system, possessing widely different time constants. Details about the method are described in Sec. 3.
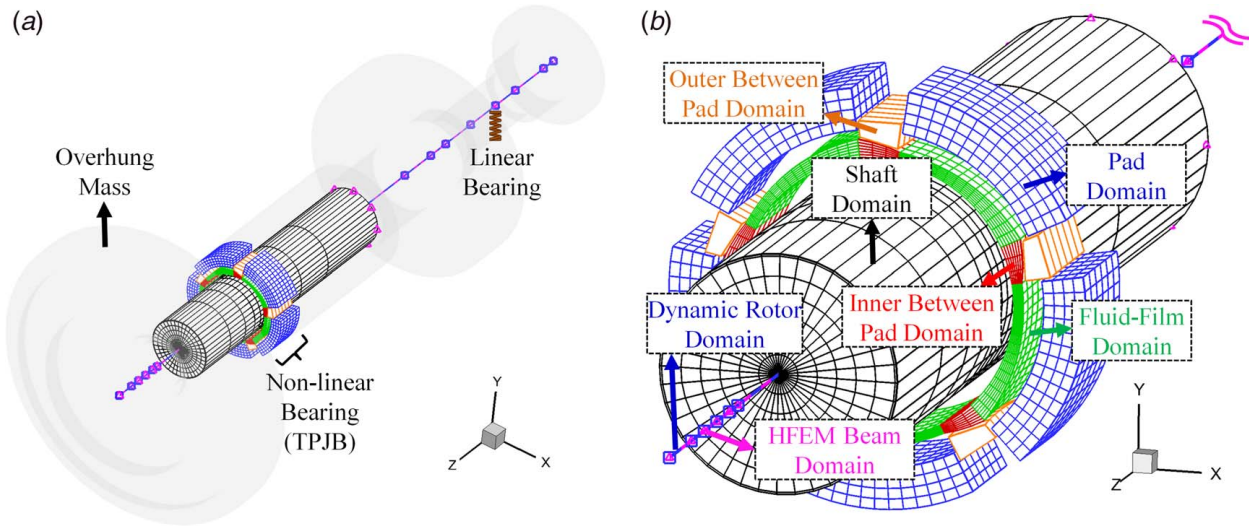
Fig. 2 Illustration of computational domain for Morton effect simulation: (a) overview and (b) magnified view

Table 1 Summary of computational domains for Morton effect simulation

Computational domain	Type	Theory	Dim.	Numerical integration		Dependent variable
				Space	Time	
Fluid-film	Fluid	Reynolds	2D	FVM	–	P
		Energy	3D	FVM	A.R.K.	T_f
Inner between pad	Fluid	Mass	3D	FVM	–	u_{IB}, v_{IB}, w_{IB}
		Energy	3D	FVM	A.R.K.	T_{IB}
Outer between pad	Fluid	Mass	1D	FVM	–	w_{OB}
		Energy	1D	FVM	I.E.	T_{OB}
Pad	Solid	T.D.	3D	FEM	–	x_{tp}, y_{tp}, z_{tp}
		D.F.P.	3D	FEM	A.R.K.	x_p, y_p, z_p
		Energy	3D	FEM	A.R.K.	T_p
Rotor (shaft)	Solid	T.D.	3D	FEM	–	x_{tr}, y_{tr}, z_{tr}
		Energy	3D	FEM	A.R.K.	T_R
HFEM beam	Solid	Euler-Beam	1D	FEM	–	$x_{tr}, y_{tr}, z_{tr}, \theta_{tr,x}, \theta_{tr,y}, \theta_{tr,z}$
Dynamic rotor	Solid	Euler-Beam	1D	FEM	A.R.K.	$x_R, y_R, \theta_{Rx}, \theta_{Ry}$
Dynamic pad	Solid	Rigid pad	0D	–	A.R.K.	x_{pvt}, δ_{tilt}

Note: Dim.: dimension, T.D.: thermal deformation, D.F.P.: dynamic flexible pad, A.R.K.: adaptive Runge–Kutta, and I.E.: implicit Euler.

The film thicknesses in the Reynolds model are continuously updated from the dynamics model displacements (x_R, y_R, θ_{Rx}, θ_{Ry}, x_p, y_p, z_p, x_{pvt}, δ_{tilt}), and the Reynolds model's pressure solutions (P) are transferred to the interface boundaries of the rotor and pad dynamics models, throughout the time integration. In addition, the Reynolds and energy equations are coupled in the fluid-film domain. The Reynolds model yields 3D velocity fields derived from the pressure solution [14]. The velocity fields are applied to the convective terms of the energy equation for updating the transient temperature field (T_f) of the fluid-film, which changes the dynamic viscosity fields in the Reynolds model.

As described in Part I, leading-edge temperatures in the fluid-film are imposed from the temperature solution (T_{IB}) of the HBP model. Transient temperatures of the pads and rotor (T_p, T_R) are calculated after the steady-state synchronous orbit is achieved. The rotor temperature (T_R) is substituted into the thermal load term in the HFEM model to obtain shaft and journal displacements (x_{tr}, y_{tr}, z_{tr}, $\theta_{tr,x}$, $\theta_{tr,y}$, $\theta_{tr,z}$, x_{tr}, y_{tr}, z_{tr}) due to thermal deformation. These displacements are used to determine the thermal imbalance and bow terms (synchronous excitation forces) in the dynamic rotor model, which are essential for simulating the ME phenomena. Modeling methods for the fluid-type domains and the boundary prescriptions are provided in Part I and are valid for the ME simulation. The theoretical models in Secs. 2.2, 2.3, and 3 are applied in a repetitive manner

during the system's transient, numerical integration-based ME solution.

2.2 Dynamic Rotor and Pad Models. Figure 3 illustrates the Euler-Bernoulli beam rotor model with force sources. The thermal imbalance/bow force sources are included in the model but not shown.

The governing equations for the rotor-bearing system are shown in Eqs. (1)–(4). The mass, damping, and stiffness matrices are $[M_R]$,
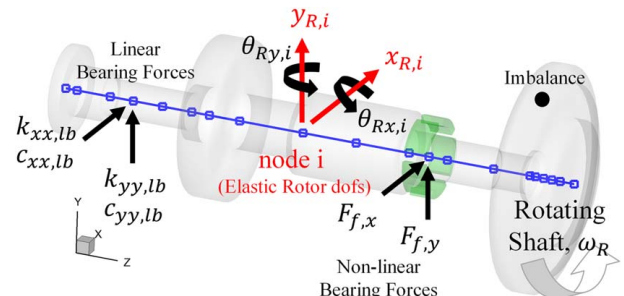
Fig. 3 Degrees-of-freedom of the elastic rotor and force sources

$[C_R]$, and $[K_R]$, respectively, and the component of the matrices are provided in the Appendix. The "damping" matrix $[C_R]$ also includes gyroscopic moment terms. The total number of the rotor nodes is n_R. The right-hand side in Eq. (1) consists of the force terms generated by the linear bearing $\{F_{lb}\}$ [30], mechanical imbalance $\{F_{im,i}\}$, and nonlinear bearing $\{F_{nb,i}\}$. The force terms are given in Eqs. (2)–(4)

$$\underset{(4n_R \times 4n_R)}{[M_R]} \underset{(4n_R \times 1)}{\{\ddot{x}_t\}} + \underset{(4n_R \times 4n_R)}{[C_R]} \underset{(4n_R \times 1)}{\{\dot{x}_t\}} + \underset{(4n_R \times 4n_R)}{[K_R]} \underset{(4n_R \times 1)}{\{x_r\}}$$
$$= \underset{(4n_R \times 1)}{\{F_{lb}\}} + \underset{(4n_R \times 1)}{\{F_{im}\}} + \underset{(4n_R \times 1)}{\{F_{nb}\}} \qquad (1)$$

$$\underset{(4n_R \times 1)}{\{F_{lb}\}} = - \underset{(4n_R \times 4n_R)}{[C_{lb}]} \underset{(4n_R \times 1)}{\{\dot{x}_t\}} - \underset{(4n_R \times 4n_R)}{[K_{lb}]} \underset{(4n_R \times 1)}{\{x_t\}} \qquad (2)$$

$$\underset{(4 \times 1)}{\{F_{im,i}\}} = \{ m_{im,i} e_{im,i} \omega_R^2 \cos(\omega_R t + \varphi_{im,i}),$$
$$m_{im,i} e_{im,i} \omega_R^2 \sin(\omega_R t + \varphi_{im,i}), \ 0, \ 0\}^T \qquad (3)$$

$$\underset{(4 \times 1)}{\{F_{nb,i}\}} = \{ F_{f,x}, \ F_{f,y}, \ 0, \ 0\}^T \qquad (4)$$

The rotor's total displacement vector $\{x_t\}$ has four degrees-of-freedom (DOFs) ($x_{R,i}$, $y_{R,i}$, $\theta_{Rx,i}$, $\theta_{Ry,i}$) for node i, the angular DOFs ($\theta_{Rx,i}$, $\theta_{Ry,i}$) follows the right-hand rule in the stationary frame, $m_{im,i}$ is the unbalance mass at node i, $e_{im,i}$ and $\varphi_{im,i}$ indicate the mechanical imbalance magnitude and phase angle, respectively, ω_R is the rotor spin frequency, and $F_{f,x}$ and $F_{f,y}$ are the forces generated by the pressure in the fluid-film of the nonlinear bearing. The total displacement vector $\{x_t\}$ is obtained from the summation of the relative displacement vector $\{x_r\}$ and thermal bow vector $\{x_{bw}\}$

$$\underset{(4n_r \times 1)}{\{x_t\}} = \underset{(4n_r \times 1)}{\{x_r\}} + \underset{(4n_r \times 1)}{\{x_{bw}\}} \qquad (5)$$

Substitution of Eq. (5) into Eq. (1), and rearranging terms yields Eq. (6). The force terms from the gyroscopic and thermal bow effects are included in Eq. (7). The gyroscopic moment terms for all nodes are given in Eq. (8). Tong et al. [16] introduced the thermal bow model to replace the previous "effective" overhung wheel imbalance [14], due to the bow model's closer resemblance to the actual ME thermal shaft bowing. This thermal bow model is applied in the present study. The force term Eq. (9) in the thermal bow model includes the thermal imbalance and bow. The mechanical imbalance $e_{im,i}$, thermal imbalance $e_{bw,i}$, and thermal bow $\theta_{bw,i}$ generate synchronous dynamic excitation at the rotor spin frequency, ω_R, and are included in Eqs. (3) and (9). The thermal imbalance and bow, including phase lag, are continuously updated at all rotor nodes when the shaft temperature is updated in the time staggered, transient numerical integration algorithm [13]

$$\underset{(4n_R \times 4n_R)}{[M_R]} \underset{(4n_R \times 1)}{\{\ddot{x}_r\}} + \underset{(4n_R \times 4n_R)}{[K_R]} \underset{(4n_R \times 1)}{\{x_r\}} = \underset{(4n_R \times 1)}{\{F_R\}} \qquad (6)$$

$$\underset{(4n_R \times 1)}{\{F_R\}} = \underset{(4n_R \times 1)}{\{F_{lb}\}} + \underset{(4n_R \times 1)}{\{F_{im}\}} + \underset{(4n_R \times 1)}{\{F_{nb}\}} + \underset{(4n_R \times 1)}{\{F_{bw}\}} + \underset{(4n_R \times 1)}{\{F_{gs}\}} \qquad (7)$$

$$\underset{(4n_R \times 1)}{\{F_{gs}\}} = - \underset{(4n_R \times 4n_R)}{[C_{gs}]} \underset{(4n_R \times 1)}{\{\dot{x}_t\}} \qquad (8)$$

$$\underset{(4 \times 1)}{\{F_{bw,i}\}} = \begin{cases} m_{R,i} e_{bw,i} \omega_R^2 \cos(\omega_R t + \varphi_{bw,i}) \\ m_{R,i} e_{bw,i} \omega_R^2 \sin(\omega_R t + \varphi_{bw,i}) \\ -I_{T,i} \theta_{bw,i} \omega_R^2 \sin(\omega_R t + \psi_{bw,i}) \\ I_{T,i} \theta_{bw,i} \omega_R^2 \cos(\omega_R t + \psi_{bw,i}) \end{cases} \qquad (9)$$

Modal reduction of the rotordynamics model is used to significantly accelerate computation speed. The relative displacement vector $\{x_r\}$ of physical coordinate is approximated by a subspace spanned by lowest frequency, free-free modal basis vectors, in columns of the eigenvector matrix $[\Phi_R]$. The modal transformation, with modal coordinate vector $\{\xi_r\}$, is substituted into (6), which is then premultiplied by $[\Phi_R]^T$. This partially decouples and condenses the mass, damping, and stiffness matrices to an order equal to the m_s selected lowest frequency modes, as follows:

$$\underset{(4n_s \times 1)}{\{x_r\}} = \underset{(4n_s \times m_s)}{[\Phi_R]} \underset{(m_s \times 1)}{\{\xi_r\}} \qquad (10)$$

$$\underset{(m_R \times 4n_R)}{[\Phi_R]^T} \underset{(4n_R \times 4n_R)}{[M_R]} \underset{(4n_R \times m_R)}{[\Phi_R]} \underset{(m_R \times 1)}{\{\ddot{\xi}_r\}} + \underset{(m_R \times 4n_R)}{[\Phi_R]^T} \underset{(4n_R \times 4n_R)}{[K_R]} \underset{(4n_R \times m_R)}{[\Phi_R]} \underset{(m_R \times 1)}{\{\xi_r\}}$$
$$= \underset{(m_R \times 4n_R)}{[\Phi_R]^T} \underset{(4n_R \times 1)}{\{F_R\}} \qquad (11)$$

Equation (11) simplifies to Eq. (12), with the eigenvalue matrix $[\lambda_R]$ in Eq. (13), the modal mass matrix $[M_{\xi,R}]$ in Eq. (14), and the modal force vector $\{F_{\xi,R}\}$ in Eq. (15). An adaptive Runge–Kutta method is applied to Eq. (12) to determine the modal coordinates $\{\xi_r\}$ which are then transformed into the physical coordinate, relative displacements $\{x_r\}$ by Eq. (10). The total (absolute), physical coordinate displacements $\{x_t\}$ are then obtained from Eq. (5)

$$\underset{(m_R \times 1)}{\{\ddot{\xi}_r\}} + \underset{(m_R \times m_R)}{[\lambda_R]} \underset{(m_R \times 1)}{\{\xi_r\}} = \underset{(m_R \times m_R)}{[M_{\xi,R}]^{-1}} \underset{(m_R \times 1)}{\{F_{\xi,R}\}} \qquad (12)$$

$$\underset{(m_R \times m_R)}{[\lambda_R]} = \underset{(m_R \times 4n_R)}{[\Phi_R]^T} \underset{(4n_R \times 4n_R)}{[M_R]^{-1}} \underset{(4n_R \times 4n_R)}{[K_R]} \underset{(4n_R \times m_R)}{[\Phi_R]} \qquad (13)$$

$$\underset{(m_R \times m_R)}{[M_{\xi,R}]} = \underset{(m_R \times 4n_R)}{[\Phi_R]^T} \underset{(4n_R \times 4n_R)}{[M_R]} \underset{(4n_R \times m_R)}{[\Phi_R]} \qquad (14)$$

$$\underset{(m_R \times 1)}{\{F_{\xi,R}\}} = \underset{(m_R \times 4n_R)}{[\Phi_R]^T} \underset{(4n_R \times 1)}{\{F_R\}} \qquad (15)$$

Both rigid and flexible pad dynamic models are used; however, flexible pads are utilized unless otherwise stated, for comparing results for rigid versus flexible pad (Sec. 6). Detailed theory descriptions for the pad dynamic models are provided in Part I, with all contents identically applicable to ME simulations.

2.3 Transient Thermal Rotor and Pad Model. Figure 4 shows the shaft and pad domains for modeling their temperature increase due to heating from the viscous heat generated in the fluid-film. This increase causes rotor and pad thermal expansions, with corresponding film thickness reductions, which could significantly impact rotor-dynamic response. Most importantly for the ME, the circumferential temperature distribution of the shaft caused by asymmetric heating creates a thermal bending moment that causes thermal bow. The 3D FEM shaft domain is coupled with the beam model to form the hybrid FEM model (HFEM). This provides a more accurate model for thermally induced bending, as opposed to a simple beam approach [16], and limits computation time increase by localizing the solid elements near to the journal. Heat conduction
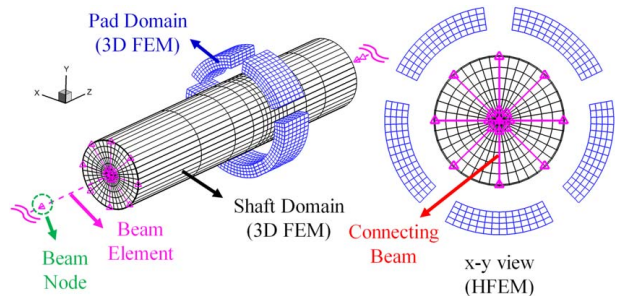
Fig. 4 Solid domains for transient thermal deformation prediction (ME Solver)

and thermal deformation are solved for the same rotor and pad domains. The temperature fields that cause the thermal deformations and bow are provided by solution of the transient heat conduction equation [16,32]

$$\rho_s \, c_{p,s} \frac{\partial T_s}{\partial t} = \nabla \cdot (k_s \nabla T_s) \qquad (16)$$

where s is the domain index of the rotor and pads, ρ_s is the density, $c_{p,s}$ is the specific heat, and k_s is the thermal conductivity of the solid.

The FEM form of the transient heat conduction equation is given by (17), where the specific heat matrix is $[C_{T,s}]$, the conductivity matrix is $[K_{T,s}]$ and the transient temperature vector for the solid is $\{T_s\}$, as discussed in the appendix of Part I. A modal reduction technique, using the thermal mode eigenvector matrix $[\Phi_s]$, is applied, and the reduced and decoupled equation is given by Eq. (18). The uncoupled differential equations in (18) are very efficiently solved with an analytical solution, since the modal force vector $\{F_{\xi,s}\}$ is based on the average heat flux over an orbit, and therefore is treated as constant in time.

Transient temperature (solid domain):

$$\underset{(n_{T,s}\times n_{T,s})}{[C_{T,s}]} \underset{(n_{T,s}\times 1)}{\{\dot{T}_s\}} + \underset{(n_{T,s}\times n_{T,s})}{[K_{T,s}]} \underset{(n_{T,s}\times 1)}{\{T_s\}} = \underset{(n_{T,s}\times 1)}{\{F_{T,s}\}} \qquad (17)$$

Modal reduction for transient temperature (solid domain):

$$\underset{(m_s\times 1)}{\{\dot{\xi}_s\}} + \underset{(m_s\times m_s)}{[\lambda_s]} \underset{(m_s\times 1)}{\{\xi_s\}} = \underset{(m_s\times m_s)}{[C_{\xi,s}]^{-1}} \underset{(m_s\times 1)}{\{F_{\xi,s}\}} \qquad (18)$$

where $[\lambda_s] = [\Phi_s]^T[C_s]^{-1}[K_s][\Phi_s]$ and $\{F_\xi\} = [\Phi_s]^T\{F_s\}$.
Deformation (solid domain):

$$\underset{(3n_s\times 3n_s)}{[K_s]} \underset{(3n_s\times 1)}{\{x_{ts}\}} = \underset{(3n_s\times 1)}{\{F_s\}} \qquad (19)$$

The temperature field obtained from the solution of Eq. (18) is substituted, as the thermal load, into the force vector $\{F_s\}$ in Eq. (19). Centrifugal force is also included in $\{F_s\}$, which was neglected in prior studies [14,16,17], and is discussed in the appendix of Part I. The displacement solutions $\{x_{ts}\}$ of the beam and 3D FEM models are utilized to calculate the thermal imbalance and bow, and phase angles $\{e_{bw}(z), \varphi_{bw}(z), \theta_{bw}(z), \psi_{bw}(z)\}^T$ in Eq. (9). These act synchronously, similarly with the excitation force sources, and can cause the thermally induced rotor instability (ME).

With reference to Fig. 5, the thermally induced imbalance and bow are given by

$$\begin{Bmatrix} e_{bw}(z) \\ \varphi_{bw}(z) \\ \theta_{bw}(z) \\ \psi_{bw}(z) \end{Bmatrix} = \begin{cases} \{e_{BM}(z), \;\; \varphi_{BM}(z), \;\; \theta_{BM}(z), \;\; \psi_{BM}(z)\}^T, \;\; 0 \le z \le z_L \\ \{e_{FE}(z), \;\; \varphi_{FE}(z), \;\; \theta_{FE}(z), \;\; \psi_{FE}(z)\}^T, \;\; z_L \le z \le z_R \\ \{e_{FE}(z_R) + (z-z_R)\tan(\beta_R), \;\; \varphi_{FE}(z_R), \;\; \beta_R, \;\; \varphi_{FE}(z_R)\}^T, \;\; z_R \le z \le z_{END} \end{cases} \qquad (20)$$

and vary according with the axial segment of the shaft considered. The critical axial locations are the starting and ending points of the 3D FEM rotor. The thermally induced imbalance 1 (e_{bw}) and thermal bow (θ_{bw}), with their phase angles (φ_{bw}, ψ_{bw}), are determined by the beam model solution when $z \le z_L$, and are calculated from the 3D FEM displacement solution if $z_L \le z \le z_R$. For z greater than z_R, the thermal imbalance and bow are determined from the assumption of constant thermal bow and phase angles ($\theta_{bw}(z) = \beta_R$, $\varphi_{bw}(z) = \psi_{bw}(z) = \varphi_{FE}(z_R)$), determined from the 3D FEM shaft domain.

3 Algorithm for Morton Effect Simulation

The ME is a highly coupled thermal-vibration phenomena that typically involves thermal responses on the order of minutes and vibration responses on the order of msecs. This disparity in time scales presents a simulation challenge to maintain accuracy while providing an economical, practical solution time. A staggered
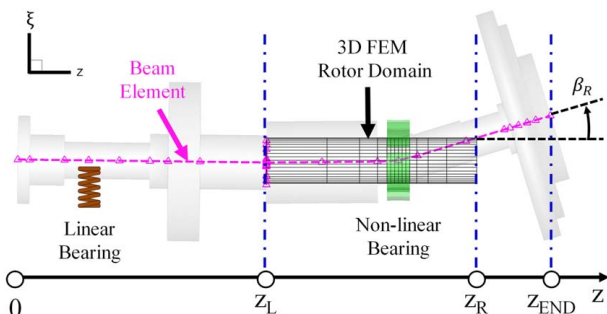
time integration scheme [13] is used as illustrated in Fig. 6, for this purpose. The underlying assumption is that the temperatures in the thermal model maintain essentially constant values over many cycles of vibration, after which they are updated. The short time scale (Δt_l, local time period) on the order of the shaft's rotation period, is applied to the rotor and pad dynamic models coupled with the Reynolds, fluid-film energy, and HBP models during the time integration. The long time scale (Δt_g, global time period) is applied for the transient solid heat conduction model and was empirically selected based on simulation studies to be 200 rotation periods [16]. In the case of the HBP model, the time integration is alternatively carried out for both local and global time periods, regarding the thermal mass of the OBP and IBP domains.

Figure 7 shows the overall algorithm for transient ME simulation. The ME simulation is started with the initialization of all dependent variables represented in Table 1. All necessary mass, stiffness, and damping matrices are assembled before the main computation begins. The eigenvalues and eigenvectors are then calculated for

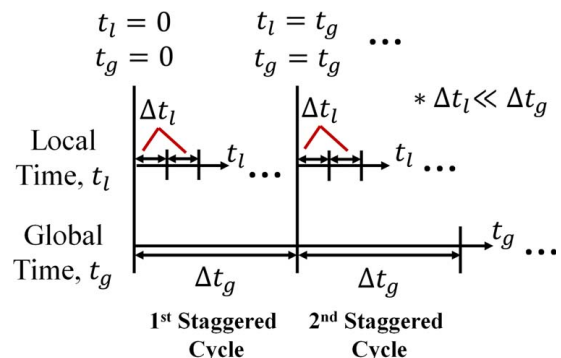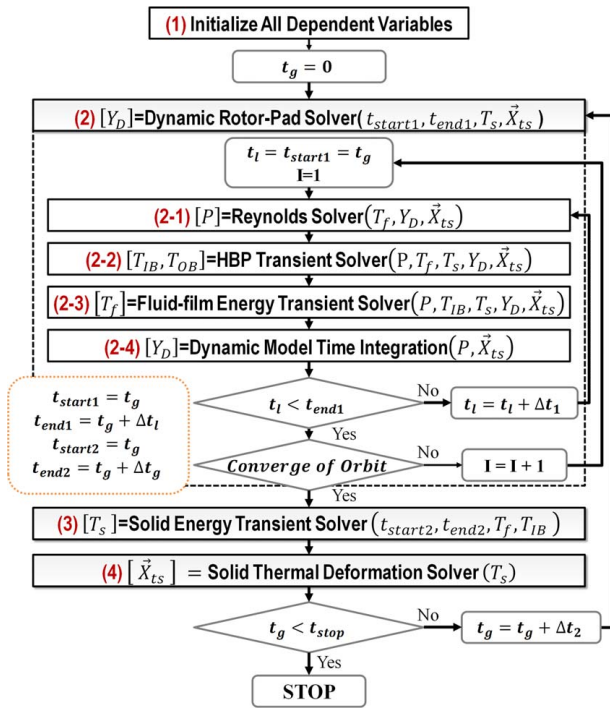Fig. 5 Illustration of HFEM for calculating thermal imbalance and bow

Fig. 6 Staggered time integration scheme

Fig. 7 Algorithm for transient Morton effect simulation

the modal reduction and transformation between the physical and modal coordinates.

The rotor-pad dynamics, coupled with the Reynolds, HBP transient, and fluid-film energy transient solvers sequentially compute their respective dependent variables to acquire a new Y_D (displacements and velocities of the rotor and pads) during the time integration. During each time-step, the h_f and $\dot{h}_f$ (film thickness and film thickness derivative), including $h_{s,TE}$ (film thickness change by thermal deformation), are estimated from the calculated Y_D and $\mathbf{X}_{ts}$ (displacement vector by thermal deformation). The h_f and $\dot{h}_f$ are the needed in all physical models of the fluid domains. Thus, Y_D and $\mathbf{X}_{ts}$ are treated as inputs in the Reynolds, HBP transient, and fluid-film energy transient solvers. Each domain is implicitly coupled with other domains, via the dependence of any domain on the calculated quantities from other domains. For instance, the Reynolds solver requires the fluid-film temperature field (T_f) for the new dynamic viscosity field $\mu_f(T_f)$. The pressure field (P) from the Reynolds solver is utilized to determine the velocity fields in the fluid-film (u, v, w) and HBP (u_{IB}, v_{IB}, w_{IB}, w_{OB}) models. Also, the HBP and fluid-film energy transient solvers share the temperature fields (T_f, T_{IB}) for the fluid–fluid-type interface boundary prescriptions, and both solvers include the solid temperature field (T_s) as an input for the fluid–solid-type interface boundary prescription.

As seen in the (2–4) process of Fig. 7, P and $\mathbf{X}_{ts}$ are applied to the force terms in the dynamic rotor and pad models. Here, $\mathbf{X}_{ts}$, as obtained from the solid thermal deformation solver, is utilized to compute the thermal imbalance (e_{bw}, φ_{bw}) and bow (θ_{bw}, ψ_{bw}), which are vital for the ME prediction. Then, the adaptive time integration of the dynamic models (adaptive time-step, Δt_1) is explicitly implemented during the local time period (Δt_l), and it produces the new Y_D. The motion vector Y_D includes the rotor's displacements and velocities (x_R, y_R, θ_{Rx}, θ_{Ry}, $\dot{x}_R$, $\dot{y}_R$, $\dot{\theta}_{Rx}$, $\dot{\theta}_{Ry}$) along with the rigid (x_{pvt}, δ_{tilt}, $\dot{x}_{pvt}$, $\dot{\delta}_{tilt}$) or flexible (x_p, y_p, z_p, $\dot{x}_p$, $\dot{y}_p$, $\dot{z}_p$) pad displacements and velocities. The time integration of the dynamic rotor and pad models is conducted for the modal coordinates. Thus, the pressure field is transformed into the modal force vector of the dynamic models. On the other hand, the motion Y_D is acquired after the transformation into the physical coordinates to apply it in all physical models of the fluid domains.

The steady-state orbit is checked for convergence [14] after the time integration for the local time period (Δt_l) is complete. After convergence is attained, the time integration of the rotor and pads energy transient solver is implemented for the global time period (Δt_g), after prescribing T_f and T_{IB} for the fluid–solid-type interface boundaries. The solids temperature field (T_s) is applied to the solid thermal deformation solver to predict $\mathbf{X}_{ts}$. Then, global time is increased by $\Delta t_g(\Delta t_2)$, etc., and the calculation processes from (2)–(4) iterates until the global time (t_g) reaches the user-defined stop time (t_{stop}). In the case of the steady-state ME solver, the steady-state HBP, fluid-film energy, and solids energy solvers are implemented, instead of the transient solvers. The global time-step is determined from the time constant evaluated from the solids domains.

Figure 8 provides expanded details for the HBP transient solver algorithm in process (2–2) of Fig. 7. The outputs of the solver are the HBP temperature fields (T_{IB}, T_{OB}) for the fluid–fluid-type boundary conditions between the fluid-film leading-edge and IBP trailing-edge. The input parameters for the HBP transient solver are P, T_f, T_s, Y_D, and $\mathbf{X}_{ts}$. The deflections and deformations Y_D and $\mathbf{X}_{ts}$ are used to update the film thickness with its derivative between pads and are applied in all HBP solvers. Also, P is utilized to impose the IBP's leading and trailing-edge velocity boundary conditions in the HBP mass solver. The η terms represent mixing coefficients MC obtained from machine learning.

Moreover, the HBP energy solver needs T_f for the fluid-film and IBP interface boundary prescriptions and T_s for the shaft and IBP interface boundary prescriptions. The calculation steps for the HBP transient solver are listed here:

(2-2-1) The HBP mass solver calculates the velocity fields ($\mathbf{U}_{IB}^0$, w_{OB}^0) for the condition of zero penetrating flow (Q_{pnt}^0).

(2-2-2) The velocity fields ($\mathbf{U}_{IB}^0$, w_{OB}^0) in the (2-2-1) process are substituted into the energy equation of the HBP model. The HBP energy solver yields the HBP's temperature fields (T_{IB}^0, T_{OB}^0). Then, the axial MC (η_o) obtained for zero penetrating flow is derived from the temperature fields.

(2-2-3) The axial MC (η_o and $\eta_{nn,o}$) calculated from the neural network are utilized to determine η_{ml} (MLAMC). The detailed theory for the MLAMC is given in Part I.

(2-2-4) The penetrating flow (Q_{pnt}) distribution is computed via Newton–Raphson iteration, to obtain zero error between the axial MC (η) for the current Q_{pnt}, and the MLAMC (η_{ml}). The Newton–Raphson solver iterates with the HBP mass and energy solvers while updating Q_{pnt}.

(2-2-5) The mass solver computes the new velocity fields ($\mathbf{U}_{IB}$, w_{OB}) from the Q_{pnt} obtained in (2-2-4) process.

(2-2-6) The HBP transient energy solver executes a fully implicit time integration. The total integration time is implemented alternately by the local time period Δt_l ($I \neq 1$) or global time period Δt_g ($I = 1$). In the case of the dynamic coefficient solver, the steady-state HBP energy solver without the time integration is used, instead of the transient solver.
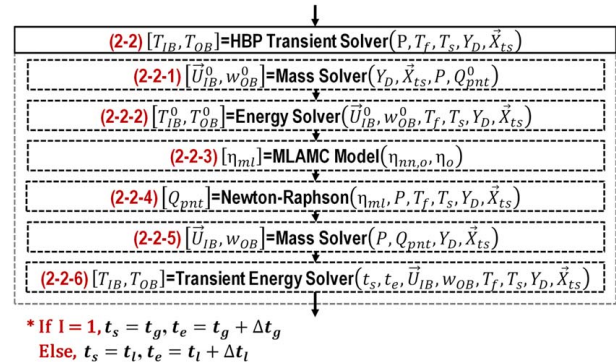
Fig. 8 HBP domain solver algorithm for transient Morton effect simulation
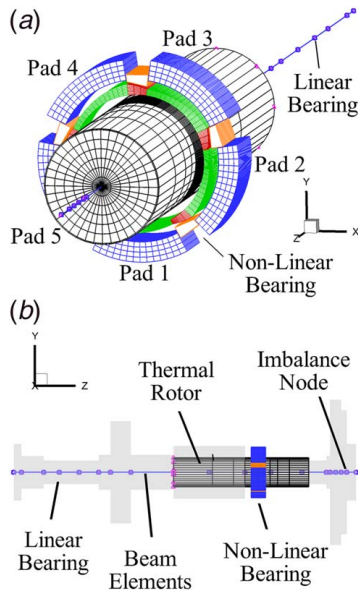
Fig. 9 Computational domain for Morton effect simulation (27,485 nodes, journal rotating direction C.C.W.): (a) TPJB view and (b) rotor view

4 Input Condition—Morton Effect Simulation

All results are obtained based on the total system geometry illustrated in Fig. 9. The number of grid nodes (27,485 nodes) in Fig. 9(a) was determined through a thorough grid convergence study. The boundary conditions for the structural model are described in Sec. 2.6 of Part I. The axial node number of the TPJB is nineteen in the FVM-HBP&MLAMC model, and seven axial nodes are utilized in the other models depending on individual grid convergences. The total number of nodes for the elastic rotor is nineteen, as indicated in Fig. 9(b). The linear and nonlinear bearings (TPJBs) are located at the 4th and 12th nodes, respectively. The mechanical imbalance is 2.74e-4 kg*m at 0 deg phase angle, at the 18th node, and is calculated so its centrifugal force is approximately 10% of the rotor weight at the planned operating speed 9400 rpm [16]. This imbalance produces a similar vibration amplitude to the experiment when the ME does not occur. The predicted

Table 2 Input parameters for the Morton effect simulation

Parameters	Value
Shaft diameter (mm)	101.6
Bearing length (mm)	50.8
Bearing radial clearance (mm)	0.0749
Number of pads	5
Pad thickness (mm)	12.7
Pad thickness at pivot (mm)	15
Pad arc length (deg)	56
Pad offset	0.5
Preload	0.5
Pivot type	Rocker (cylindrical)
Load type	Load on pad (LOP)
Outside H.C.C. (W/m²K)	50 (Shaft), 500 (Pad)
Ambient temperature (°C)	30 (Shaft), 55 (Pad)
Supply oil temperature (°C)	50
Lubricant	ISO 32
Material (solid domains)	Steel
Kxx (N/m) (linear bearing)	1.7e8
Kyy (N/m) (linear bearing)	1.7e8
Cxx (Ns/m) (linear bearing)	1.0e5
Cyy (Ns/m) (linear bearing)	1.0e5

Note: H.C.C.: heat convection coefficient.

peak-to-peak amplitude at the rotor-end is 30 μm, and the observed amplitude in the test is around 35 μm at 7500 rpm. The input parameters are listed in Table 2 and are taken from the experimental ME work in Ref. [29] for comparison. These input parameters have been utilized in several prior studies [10,14,16]. The heat convection coefficient of the outer pad surfaces is re-evaluated reflecting the trend from recent research [31].

5 Comparison With Finite Element Method—Morton Effect Simulation

By its very nature involving thermally induced shaft bow, ME simulations require very accurate journal temperature prediction. As described in Part I, a weakness of the conventional FEM film simulation is the irregular occurrences of film temperature discontinuities near the shaft surface, indicating failure of local energy conservation. This can greatly affect journal temperature prediction which depends on heat flux from the film. To illustrate this, Fig. 10 shows the FEM results with film temperature discontinuity, and FVM results without film temperature discontinuity problems.

These results are obtained for the conditions of constant 80 °C shaft and 60 °C pad surface temperatures, after 15 s simulation time. The fluid-film leading-edge temperature and pressure are 60 °C and 132 kPa, respectively. The temperature discontinuity occurs in the FEM solver for all pads, as shown by the circles in Fig. 10(a). This anomaly with the FEM solution is grid independent and adversely affects the journal temperature predictions, which depend on heat flux from the film. The negative consequences of this weakness are acute in the ME simulation which requires accurate journal asymmetric temperature distributions. The present work remedies this problem by use of a highly efficient FVM solver that enforces local energy conservation.
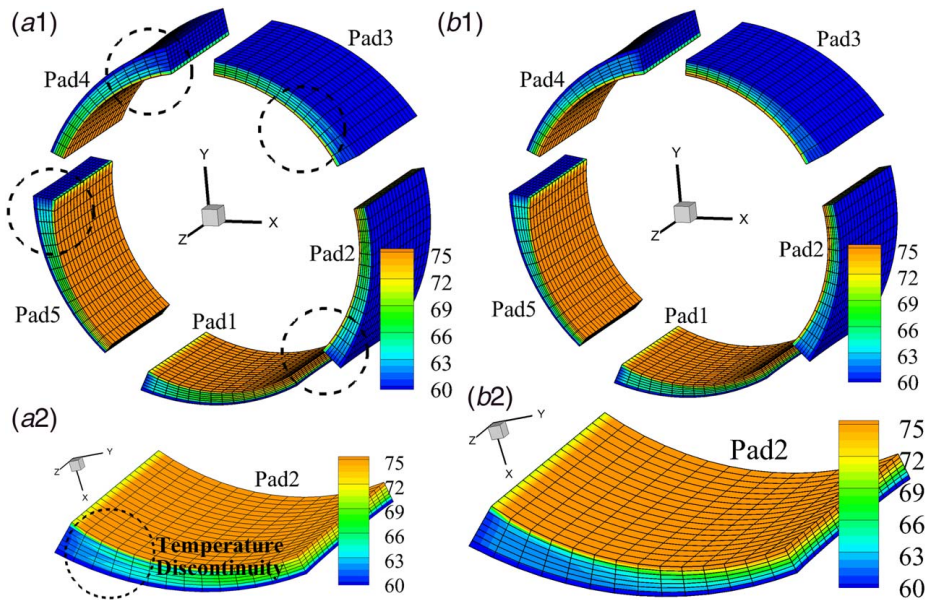
6 Morton Effect Simulation—Model Validation

6.1 Summary of Experimental Work. Test results from the key experimental work in Ref. [29] are utilized to validate the present approach. As shown in Fig. 11, there were two main tests in the study. The first test was conducted during the commissioning at the site. The second test was carried out at a testbed for reproducing the ME in the first test. An actual impeller and casing were installed for natural gas compression at low temperature (5 °C), in the first test. In contrast, the impeller was replaced with a dummy equivalent mass, and the cartridge was removed for the second test. The clearance was correspondingly decreased to compensate for the cartridge shrinkage from the cooling effect of the process gas.

Both tests in Fig. 11 are considered for validation of the present theoretical model. The critical speed of the first forward rotor mode has been calculated to occur in the 7000–8000 rpm range in Refs. [10,15,29]. A thermally induced ME instability occurred near the critical speed, did not occur below 7200 rpm, and always occurred from 8500 rpm to the maximum operating speed 9400 rpm. Therefore, transient ME simulations were performed at 7000, 9000, 9200, and 9400 rpm in Sec. 5.3, to check accuracy and compare with the conventional approaches. In addition, steady-state ME simulation results are presented in Sec. 5.4 over a wide range of operating speeds from 5000 to 12000 rpm.

There have been two prior nonlinear transient analysis ME papers [14,16] that compared predictions with the test data [29]. However, the previous studies

– did not consider the centrifugal force of the shaft and pad flexibility
– used the FEM for the discretization of the Reynolds and energy equations in the fluid-film domain and
– used a constant (uniform) MC approach for determining the fluid-film leading-edge temperature.

Fig. 10 Temperature discontinuity observed in Morton effect simulation with (a) FEM and alleviated with (b) FVM
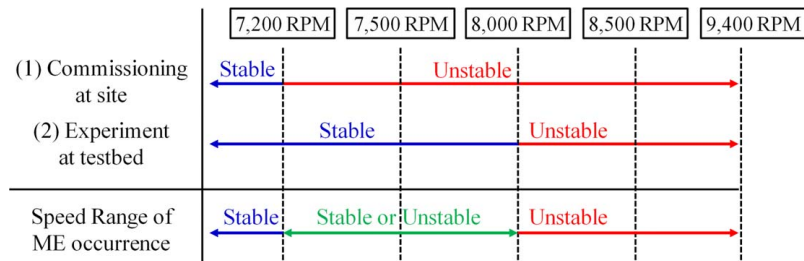
Fig. 11 Summary of the ME experimental study
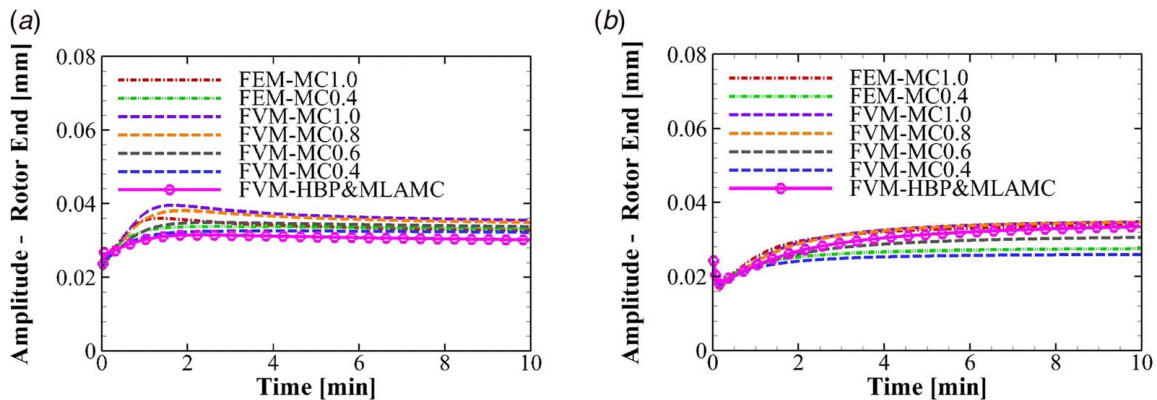
Fig. 12 Peak-to-peak vibration amplitude at the rotor end without ME: (a) 7000 rpm and (b) 9000

The drawback of the FEM was pointed out in Sec. 4. The MC approach utilized guessed MC with extremes 0.4 and 1.0 [26] and neglected the 2D variation of temperature at the fluid-film leading-edge [27]. Furthermore, the prior studies did not try to verify the model above 9000 rpm. The weaknesses of the FEM with constant MC approach for the ME prediction are illustrated in Sec. 5.3.

6.2 Dynamic Simulation Without Morton Effect. This section provides transient simulation results, without ME modeling features, for operating speeds 7000 rpm and 9000 rpm. The meaning of "without ME" implies ignoring thermal imbalance

and bow in the rotordynamics model. The purpose of the simulation is to compare the FEM-MC, FVM-MC, and FVM-HBP&MLAMC for a small orbit (no ME) case. The FEM and FVM are discretization methods for solving boundary value problems, including the Reynolds and energy equations. Uniform mixing coefficient (MC) is a conventional approach to estimate the fluid-film leading-edge temperature [14,26]. The HBP&MLAMC includes a 3D between pads, thermal fluids model, combined with machine learning axial MC, MLAMC, and is discussed in detail in Part I.

Figure 12 shows the peak-to-peak vibration amplitude at the rotor end at 7000 and 9000 rpm, neglecting ME. All modeling techniques
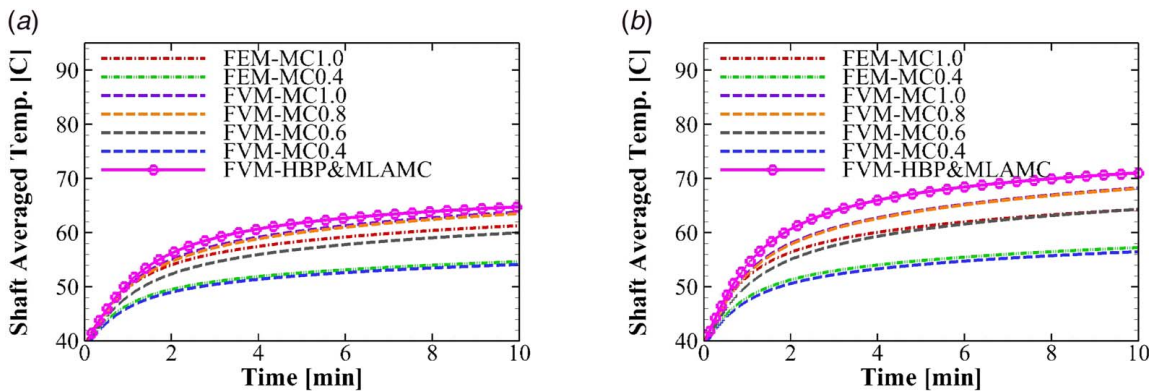
Fig. 13 Shaft averaged temperature without ME: (a) 7000 rpm and (b) 9000

show similar tendencies and values at 7000 rpm in Fig. 12(a). Figure 13(a) shows that this may be explained by the relatively small temperature variation between the methods. The temperatures shown in Fig. 13(a) are averaged over the "thermal rotor," which is the solid element shaft model in Fig. 9. Figure 13(b) shows a wider variation of shaft temperatures at the higher speed 9000 rpm, with increased viscous heating. This affects the shaft thermal expansion, bearing clearance, and bearing stiffness and damping. Thus, the amplitude in Fig. 12(b) shows a larger variation depending on the modeling approach.

The steady-state results in Fig. 13 indicate that the FEM-MC predicts cooler temperatures than the FVM-MC, except for the MC0.4 case. This results from the temperature discontinuity problem with FEM. Also, the MC approach predicts a cooler shaft than the HBP&MLAMC model due to ignoring the radial temperature distribution effect of the fluid-film, at the pad leading-edge. Table 3

Table 3   Summary of steady-state amplitudes and temperatures without ME

	Amplitude—rotor end (mm)		Shaft averaged temp. (°C)	
	7000 rpm	9000 rpm	7000 rpm	9000 rpm
FEM-MC1.0	0.0328	0.0284	61.2	64.7
FEM-MC0.4	0.0332	0.0240	54.6	57.7
FVM-MC1.0	0.0355	0.0289	63.7	69.1
FVM-MC0.8	0.0349	0.0289	63.4	69.0
FVM-MC0.6	0.0338	0.0263	59.9	65.1
FVM-MC0.4	0.0322	0.0229	54.1	56.9
FVM-HBP&MLAMC	0.0302	0.0287	64.7	72.4

summarizes the steady-state amplitudes and temperatures from Figs. 12 and 13. Circumferential temperature differences (ΔT) are plotted versus time in Fig. 14. The ΔT is defined by the difference in maximum and minimum journal surface temperatures at the bearing mid-span. As shown in Fig. 14(a), all models produce similar values, except for the FEM-MC1.0 case, at 7000 rpm. The differences become more distinguishable at the higher operating speed 9000 rpm, as shown in Fig. 14(b). The model's accuracy for shaft temperature prediction becomes more significant for higher operating speeds.

6.3   Dynamic Simulation With Morton Effect. The transient response was conducted with ME for a total simulation time of 10 min. The initial temperature of the solid domains is 40 °C, and the initial journal positions are at 0.2 eccentricity ratio and 0 deg attitude angle. The operating speed is maintained constant for each simulation. The supply oil flow is 15 LPM, and the theory for the supply oil flow is discussed in Part I. All modeling approaches show similar quantitative and qualitative results at 7000 rpm, as shown in Fig. 15(a). In contrast, the relatively large orbits appear at the higher operating speeds (9000, 9200, 9400 rpm), as shown in Figs. 15(b)–15(d). Each modeling method predicts different rotor-dynamic behaviors, with different ME growing and shrinking rates. The FVM-based methods agree with the experimental data [29] at the given operating speeds. In the tests, it was clear that the instability did not occur below 7000 rpm, but occurred from 8500 rpm to 9000 rpm. The FEM-based methods clearly do not show ME instability at the higher speeds, where tests and FVM do show ME. This demonstrates the higher accuracy of FVM over FEM for ME prediction. A reason for this could be the film temperature discontinuity shortcoming with FEM.
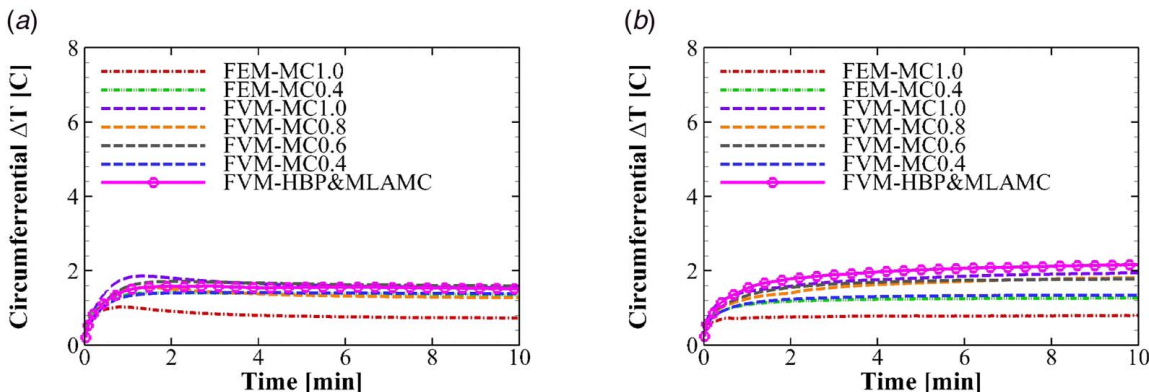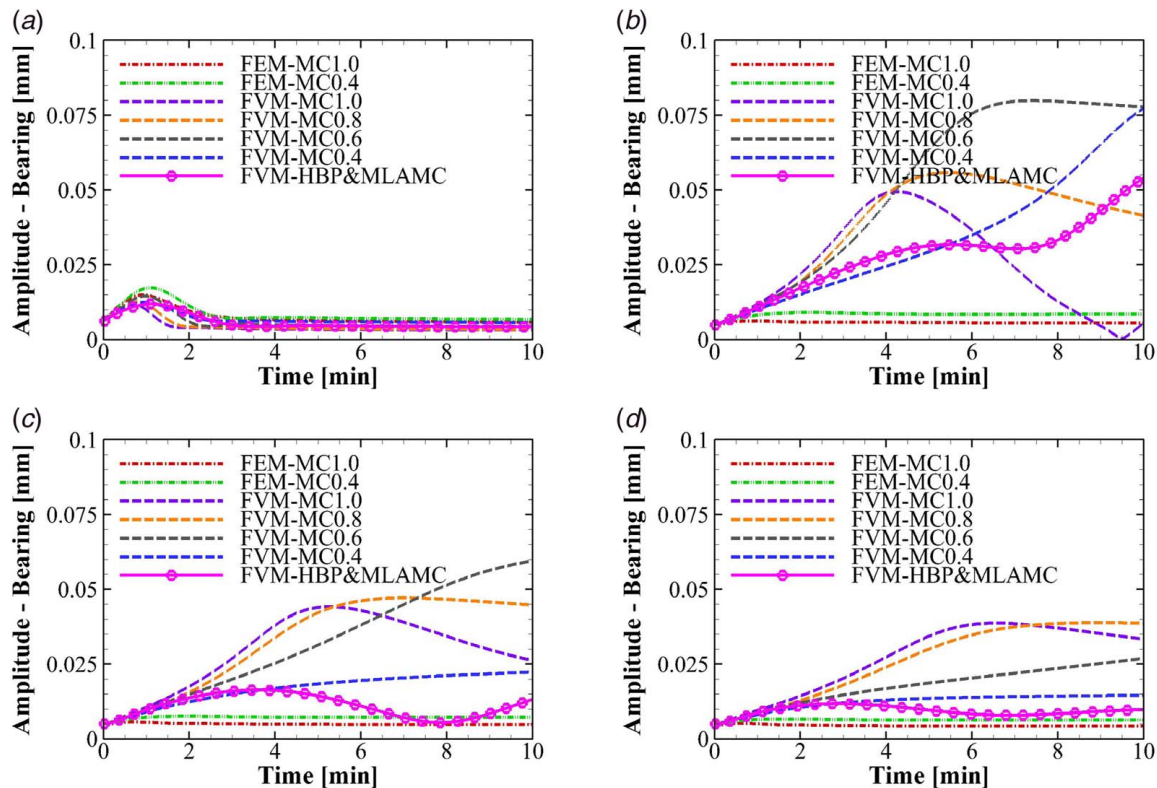

Fig. 14   Circumferential temperature difference (ΔT) without ME: (a) 7000 rpm and (b) 9000 rpm

Fig. 15 Peak-to-peak vibration amplitude at the nonlinear bearing including ME: (a) 7000 rpm, (b) 9000 rpm, (c) 9200 rpm, and (d) 9400 rpm

Figures 15(b)–15(d) show a considerable variation in response according to the selection of MC, utilizing the FVM-MC method. This demonstrates the significant uncertainty inherent in using a guessed, uniform MC based model, even with FVM. Uniform MC models neglect the radial and axial temperature distributions at the fluid-film leading-edge, which may significantly affect the predicted heat flux from the film into the journal. On the contrary, the FVM-HBP&MLAMC removes the guessed MC uncertainty and ensures temperature continuity between pads. The FVM-HBP&MLAMC ME prediction shows good agreement with the experimental work [29]. Figure 15 shows that the amplitude magnitude rapidly decreases above 9000 rpm. Thus, it can be inferred that a "stability recovery speed" [18] exists near 9400 rpm. Figure 16 shows the peak-to-peak amplitude at the rotor end. The amplitude scale is more significant than that at the TPJB. However, the tendencies are consistent in terms of the modeling approaches.

Synchronous orbiting of the journal caused by 1×, typically imbalance, excitation causes the journal to experience asymmetric heating, and, consequently a circumferential temperature difference (ΔT). The ΔT thermally bends the shaft, and the resulting thermal imbalance and bow may generate a synchronous rotor instability, also known as, the ME. Figure 17 shows ΔT predictions that are approximately proportional with the vibration amplitudes in Figs. 15 and 16. This appears to results from the ΔT creating the shaft bow that excites the vibrations. The variation of responses between the methods may also be attributed to the variations in the predicted temperature distributions, due to changes in MC values or approach.

Figures 18 and 19 show the shaft averaged temperature and temperature distribution results, respectively, for the different modeling approaches. The FVM- and FEM-based shaft averaged temperatures show a strong disagreement especially for higher MC. This is coincident with increasing temperature discontinuities for the FEM approach, as MC increases. Also, the disparity of the shaft averaged temperature prediction indicates that heat transfer

between the fluid-film and shaft can be misestimated if the classical FEM with guessed MC is applied to the ME simulation.

There is no temperature discontinuity problem in the FVM-MC model, but three vulnerabilities still occur: (1) notable MC uncertainty, (2) neglect of the 2D temperature distribution at the fluid-film leading-edge, and (3) neglect of the transient effect between pads. Figures 19 and 20 show temperature contours for each fluid and solid domain, for the FVM-MC0.8 and FVM-HBP&MLAMC models. The contours are taken at the instant when the hot spot is located at a 90 degree angular position. All prior MC approaches assume the fluid-film leading-edge temperature is constant in the radial direction as shown in Fig. 19(a). The FVM-HBP&MLAMC model considers the radial temperature distribution and maintains its continuity from the prior pad via the 3D HBP model. Furthermore, the FVM-MC model predicts higher temperatures at the bearing mid-span due to the constant MC along the axial direction, as represented in Figs. 19(a) and 20(b). In contrast, a lower temperature is calculated in the advanced model by the axial MC variation effect, which also affects the axial shaft temperature distribution, as seen in Fig. 20(b). The temperature near the oil inlet is cooled compared with the other regions [27,28].

The MC approach neglects temperature continuity between pads and assumes complete mixing for the next pad leading-edge temperature of the fluid-film. Thus, hot oil near the shaft surface experiences a forced cooling effect by the complete mixing assumption when passing through the between pad (BP) region. Thus, the averaged shaft temperature in the FVM-MC model is lower than in the FVM-HBP&MLAMC model, as shown in Fig. 18. This MC modeling weakness in turn lowers the accuracy of the ME predictions.

A key feature of the ME is the relation between high and hot spots. Generally, it is known that the hot spot lags the high spot by approximately (0–60 deg), when the ME occurs with continuous change of these phase angles [5]. Figure 20 shows the high and hot spots of all models converge to certain values at 7000 rpm. However, at higher speed and vibration amplitude, continuous
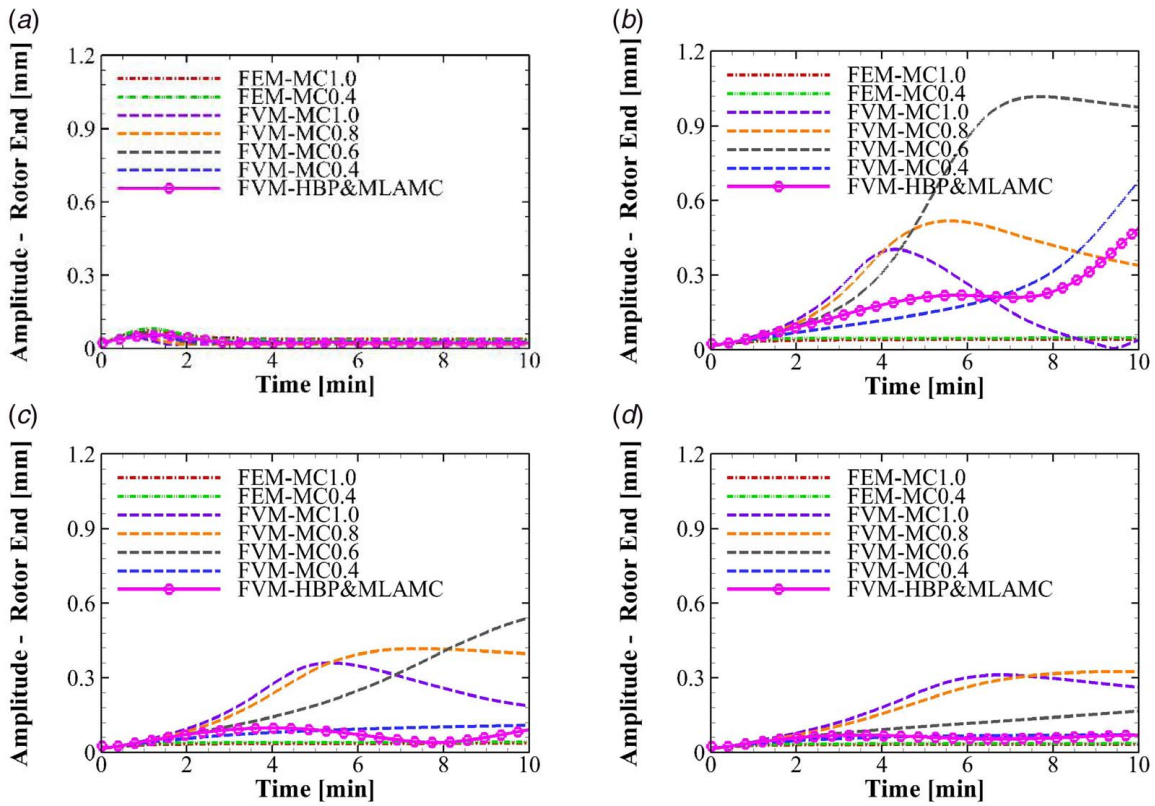
Fig. 16 Peak to peak amplitude at rotor end: (a) 7000 rpm, (b) 9000 rpm, (c) 9200 rpm, and (d) 9400 rpm
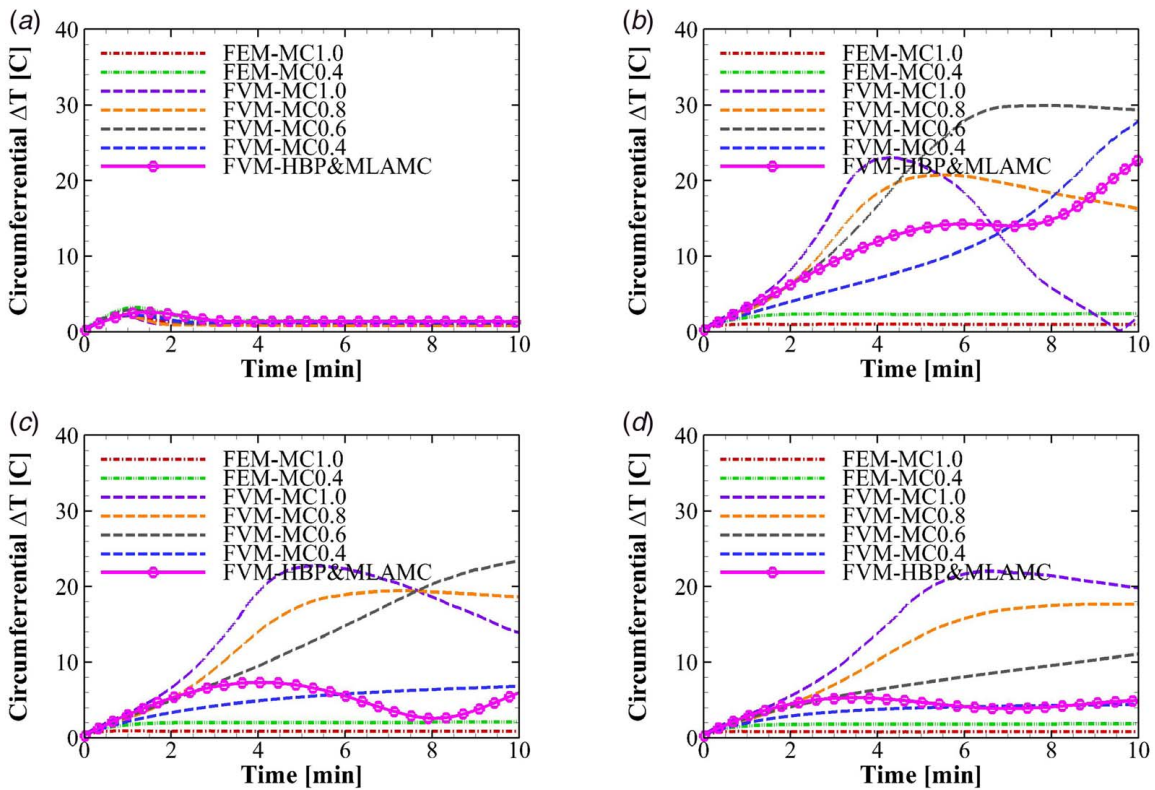

Fig. 17 Circumferential journal temperature difference (ΔT): (a) 7000 rpm, (b) 9000 rpm, (c) 9200 rpm, and (d) 9400 rpm
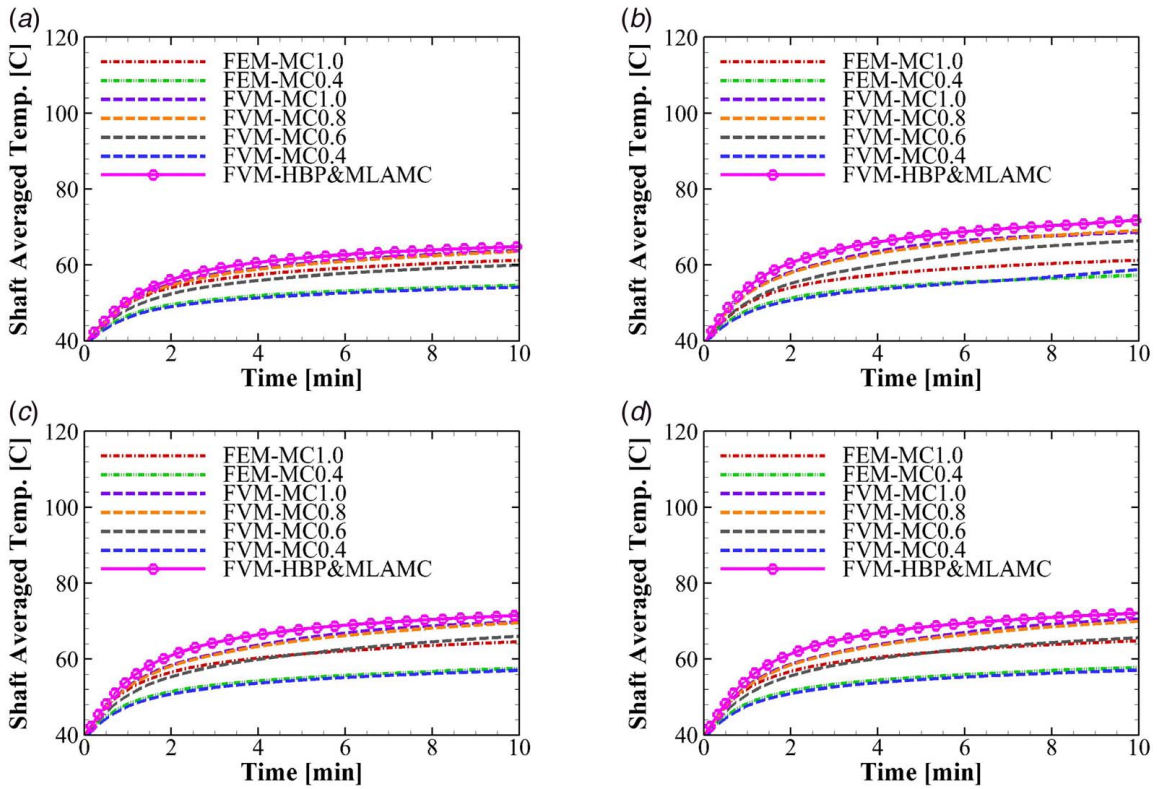
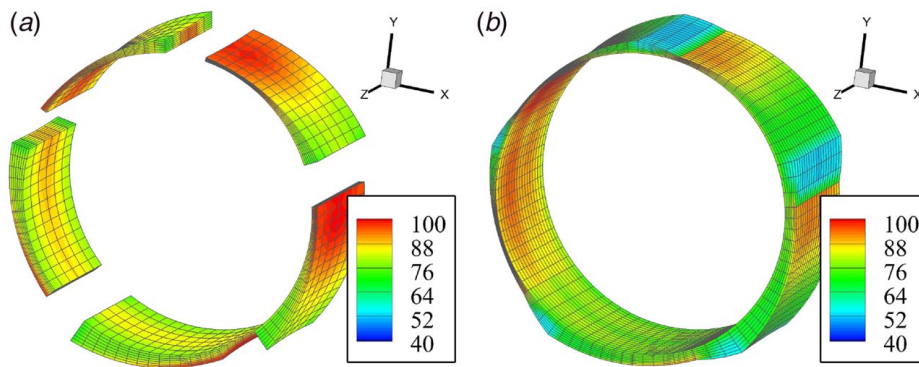**Fig. 18 Shaft averaged temperature: (a) 7000 rpm, (b) 9000 rpm, (c) 9200 rpm, and (d) 9400 rpm**

Fig. 19 Temperature contours overlaid on the deformed fluid domains at 9000 rpm (10 min and hot spot near 90 deg): (a) FVM-MC0.8 and (b) MLAMC-HBP&MLAMC
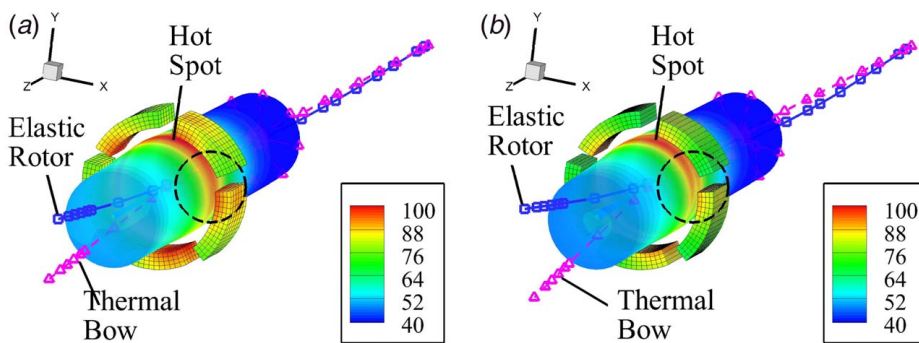

Fig. 20 Temperature contour and deflected solid domains at 9000 rpm (10 min, hot spot at 90 deg): (a) FVM-MC0.8 and (b) MLAMC-HBP&MLAMC
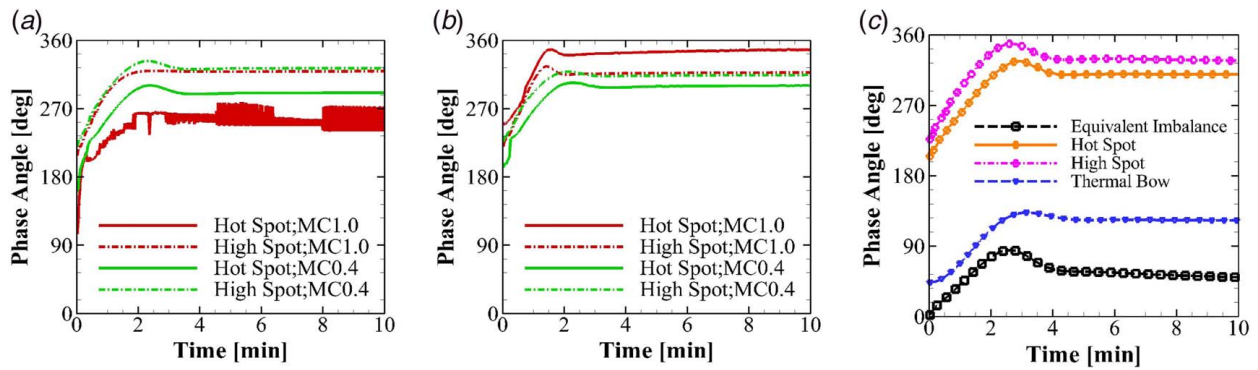
Fig. 21 Phase angle of hot and high spots at 7000 rpm: (a) FEM-MC, (b) FVM-MC, and (c) FVM-HBP&MLAMC with plot of thermal bow at the rotor end

variations of the high and hot spots are observed in the FVM-1.0MC and FVM-HBP&MLAMC solutions, as shown in Figs. 22(b) and 22(c). Figures 21(a) and 22(a) show erratic behavior of the FEM hot spot prediction which results from the failure of local energy conservation. The difference in the phase angle between hot and high spots is dependent on the MC assumption. For instance, a hot spot of MC1.0 leads the high spot, but the hot spot with MC0.4 lags behind the high spot, as shown in Fig. 22(b).

Additionally, the new model's thermal bow and equivalent imbalance is plotted in Figs. 21(c)–22(c). The thermal bow phase angle has around a 180 deg difference with the hot spot. The mechanical unbalance is located at the 0 deg phase angle. Figure 23 clearly shows that the assumed MC has a significant effect on the phase angle difference ($\Delta\emptyset$) between high and high spots. The phase angle difference increases with decreased MC for the speeds shown. The hot spot location is affected by the thermal convective effect in the circumferential direction and temperature continuity between pads. A strong convective effect means there are minor changes in the temperature when the oil fluid is transported from the prior pad to the next pad. High MC corresponds to a strong convective effect which tends to move the hot spot in the rotation direction, as shown in Figs. 23(a)–23(c). The hot spot leads the high spot for high MC, and the hot spot follows the high spot for low MC. These results show that the MC strongly determines the high spot—hot spot phase difference, if the MC approach is utilized for ME prediction. Hence, a wrong assumption for the MC value may provide misleading results for ME prediction.

In contrast, the FVM-HBP&MLAMC model utilizes radially and axially varying prescribed temperatures at the pad inlets, and yields results in reasonable agreement with experimental ME measurements [29]. The phase angle of the hot and high spots vary continuously, and the hot spot tracks the high spot in Fig. 22(c). The positive values of $\Delta\emptyset$ indicates the hot spot lagging behind the

high spot for all speeds in Figs. 23(a)–23(c). The above results show that the numerical modeling approach may have a considerable influence on the predicted ME ΔT and $\Delta\emptyset$. The widely varying responses are more readily evident in the polar plot format of Figs. 24(a) and 24(b), corresponding to 7000 and 9200 rpm, respectively. Figure 24(b) shows that the widely viewed as uncertain, selection of the MC, yields a large uncertainty in the predicted ME response, and the MC approach predictions may greatly differ compared with the higher fidelity FVM-HBP-MLAMC approach.

Figure 25 provides a visualization aid to illustrate the ME phenomenon, in particular the high spot—hot spot relation, and the circumferential temperature gradient around the journal. Scale adjustments are used to accent these effects at 9000 rpm. The synchronous steady-state orbit is the displacement solution for the elastic rotor, and the deflected rotor indicates the high spot direction. The thermal solution for the HFEM solid-beam structure provides the journal radial growth, thermal imbalance, and rotor bow. Comparison of the deflected rotor direction and peak temperature confirms that the journal surface's hot spot lags the high spot, consistent with the trend indicated in Fig. 22(c). The thermal bow (thermal rotor) orbits at an angle 180 deg from the hot spot angle.

6.4 Steady-State Simulation With Morton Effect. This section presents steady-state results to compare modeling methods and correlate with experimental ME measurements [29], over the speed range 5000–12,000 rpm. The simulation results are compared with the results obtained in a previous study [16], which neglected the spatial variation of fluid temperature at the pad leading-edge, and used the FEM for solving the Reynolds and Energy equations. Figure 26 explains the steady-state Morton simulation algorithm,
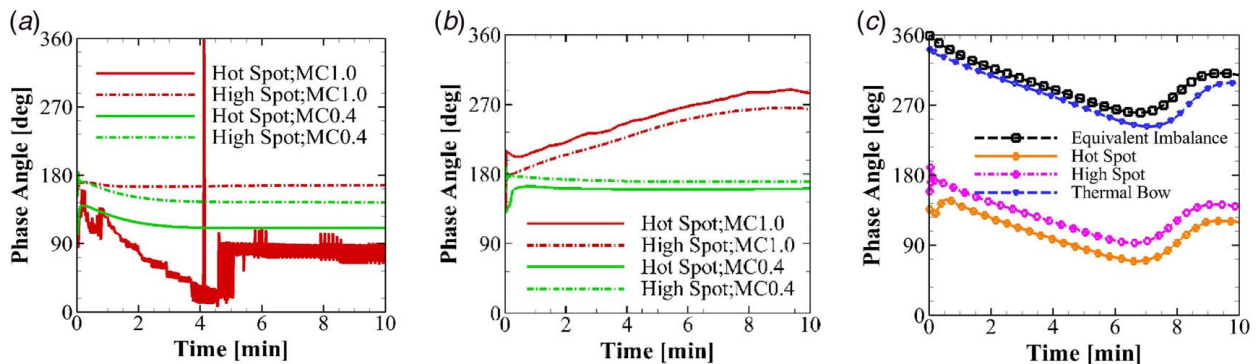

Fig. 22 Phase angle of hot and high spots at 9200 rpm: (a) FEM-MC, (b) FVM-MC, and (c) FVM-HBP&MLAMC with plot of thermal bow at the rotor end
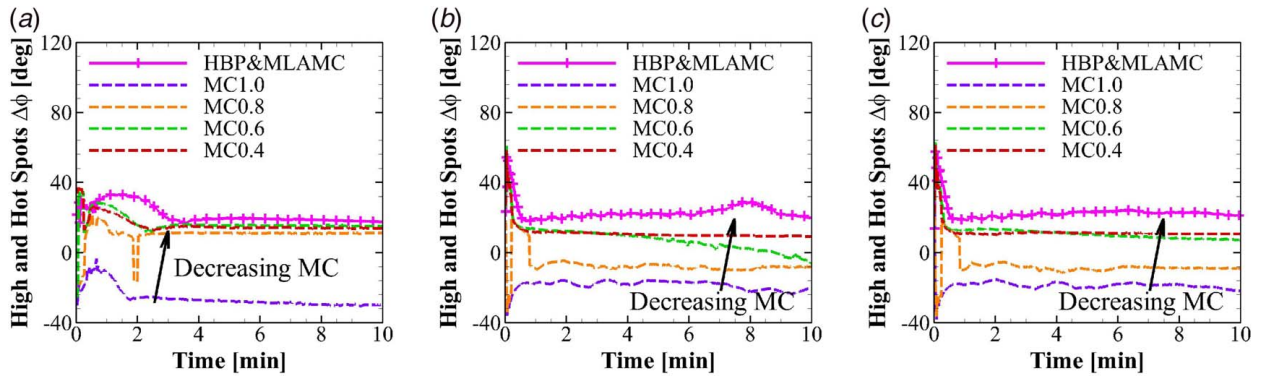
Fig. 23 Phase angle difference (Δ∅) of hot and high spots: (*a*) 7000 rpm, (*b*) 9200 rpm, and (*c*) 9400 rpm
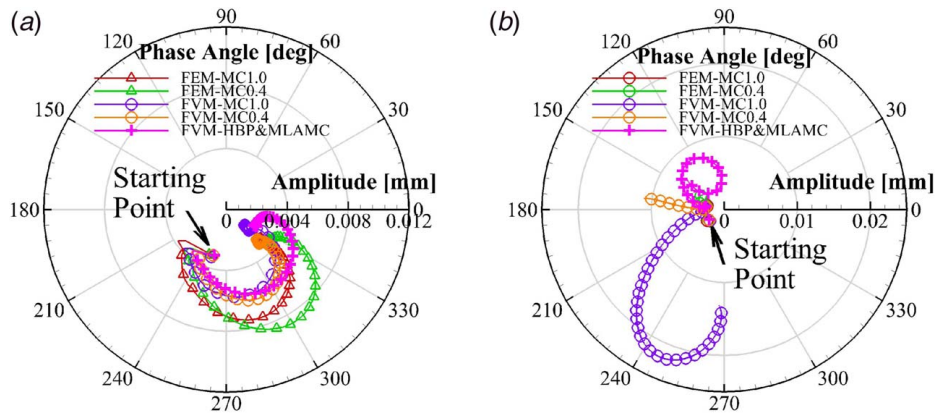

Fig. 24 1× filtered polar plot in the TPJB at (*a*) 7000 rpm and (*b*) 9200 rpm
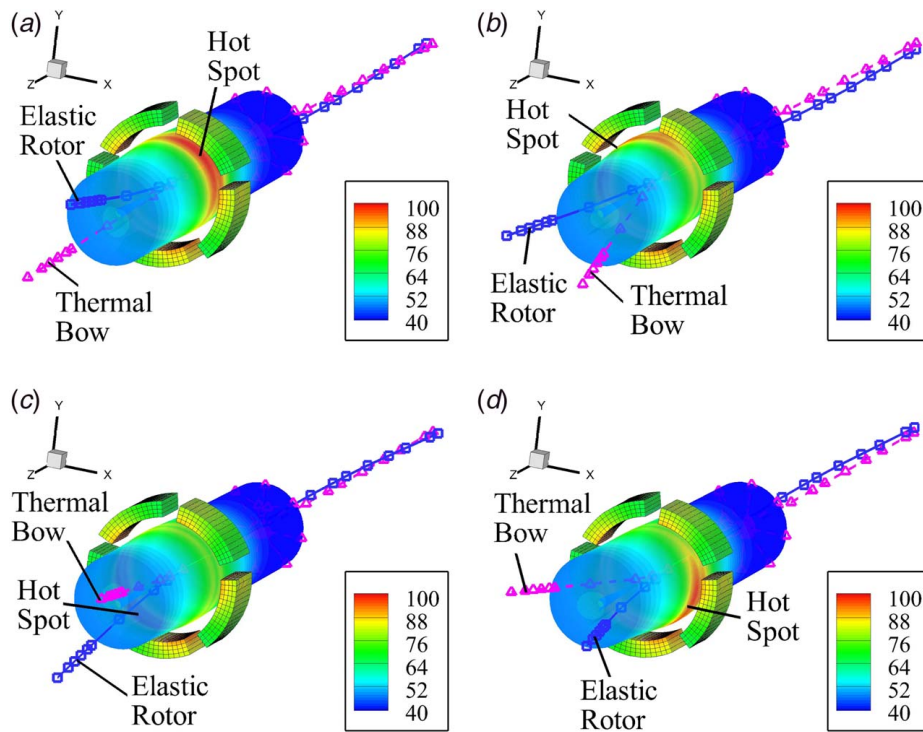

Fig. 25 Temperature contours and displacement solutions for solid domains in FVM-HBP&MLAMC at 9000 rpm (10 min): (*a*) 1/4 Period, (*b*) 2/4 Period, (*c*) 3/4 Period, and (*d*) 1 Period
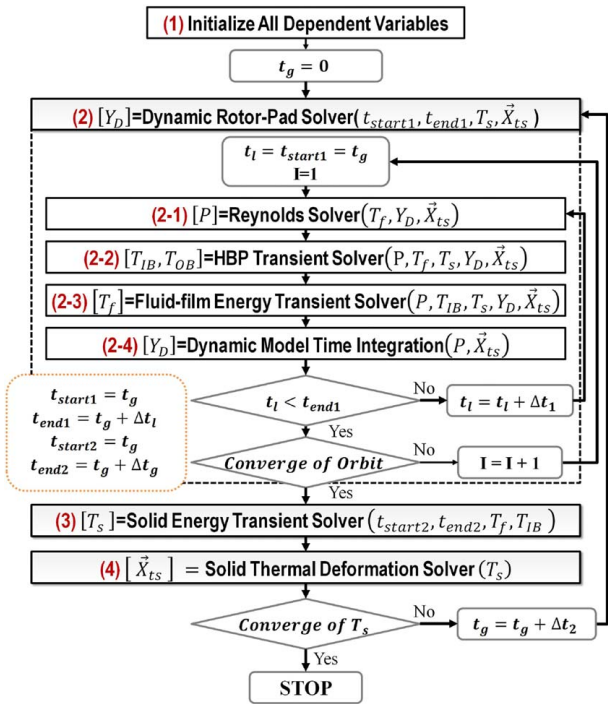
Fig. 26 Steady-state Morton effect simulation

Table 4 Comparison of steady-state and transient Morton solvers

	Steady-state Morton solver	Transient Morton solver
Time integration scheme	Staggered	
Global time-step, Δt_g	$100 \times (\rho_s c_{p,s} L_s/k_s)$	$200 \times (2\pi/\omega_R)$
Convergence criteria (Global loop)	Error of solid domain temperature	Total time

Note: Time constant (solid domain): $\rho_s c_{p,s} L_s/k_s$ and rotation period (shaft): $2\pi/\omega_R$.

domain temperatures converge. The steady-state approach reduces computation time by evaluating steady-state modal coordinate temperatures with analytical solutions of (12), utilizing the constant, orbit averaged value of the heat source term $\{F_{\xi,R}\}$. Also, by reducing the number of iterations of the global loop, the steady-state approach exchanges a reduction in resolution of the dynamics prediction for the benefit of a significant reduction in computation time.

Figure 27 shows the "FVM-HBP&MLAMC" model predictions, both with and without the ME. A large increase in vibration amplitude and/or ΔT accompanying the "with" ME model, relative to the "without" ME model, confirms the occurrence of a strong ME. As discussed in Sec. 5.1 (Fig. 11), the ME was not observed below 7200 rpm, and it was always observed above 8000 rpm.

Figures 27(a) and 27(b) show that the FVM-based models have a large amplitude and circumferential temperature difference above 9000 rpm, which agrees with the experimental results. Figure 27(d) shows a large decrease in minimum film thickness when the ME occurs, consistent with the vibration increase. The FEM approaches, including the results of the previous study [16], predict ME occurrence only near 8000 rpm, which is inconsistent with measurements (Fig. 11). Figure 27(c) shows that the FEM approach predicts cooler journal temperature, consistent with the

which is almost identical to the calculation procedure of the transient Morton solver shown in Fig. 27.

Table 4 shows that the steady-state Morton solver uses a much longer solid domain temperature update time than the transient Morton solver. The computation is terminated when the solid
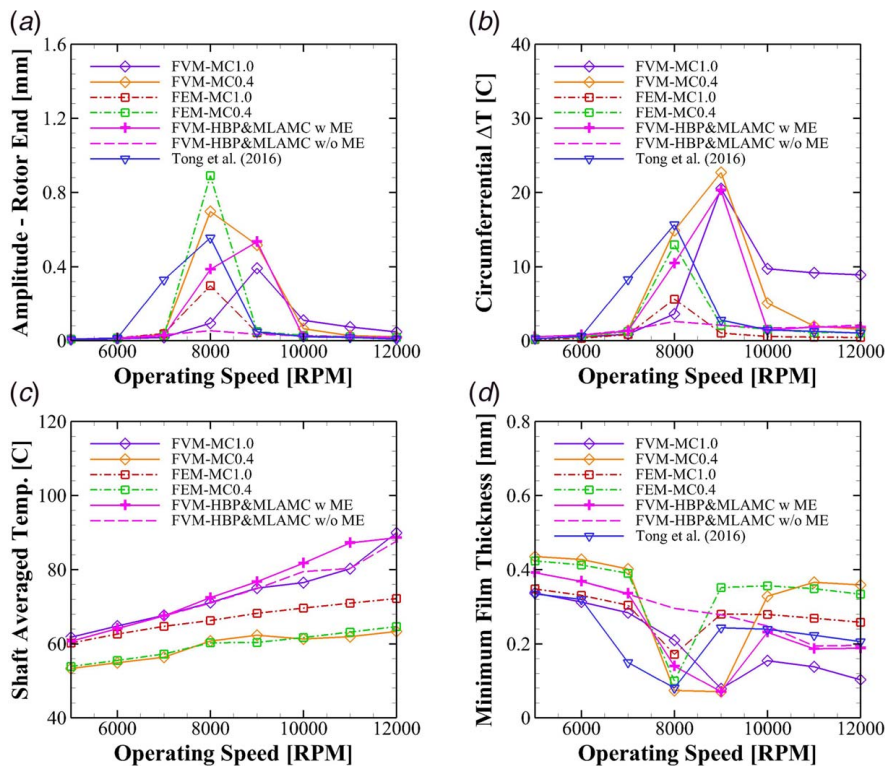

Fig. 27 Steady-state ME simulation results and comparison with (FEM-MC approach) from Ref. [16]: (a) peak to peak amplitude at rotor end, (b) maximum circumferential temperature difference at journal mid-plane, (c) thermal rotor averaged temperature, and (d) minimum film thickness

results in the transient ME simulation. The cooler journal temperature results from the constant inlet temperature assumption with the FEM approach which prevents radial heat flow into the journal and due to the temperature discontinuity problems as illustrated in Fig. 19 of Part I.

The FVM-MC results show more accuracy than the FEM-MC models, based on comparison with experimental trends. However even the FVM-MC approach has the major drawback of MC value uncertainty. Section 5.3 showed that rotor behavior depends significantly on MC, since ΔT and $\Delta \varnothing$ are strongly dependent on MC and temperature distribution at the fluid-film leading-edge. Figure 27 shows that the FVM-MC approach predicts overly cool shaft temperature compared with the higher fidelity FVM-HBP&MLAMC model. The novel FVM-HBP&MLAMC approach is recommended since it overcomes the weaknesses of the FEM-MC and FVM-MC approaches and shows better agreement with the very pauce ME experimental data.

Compared with previous approaches, the new approach provides a more accurate representation of the temperature distribution at the pad inlet, which has a significant influence on the shaft temperature, a key factor in modeling the Morton effect. The resulting effect was shown to be a broader speed range for predicted Morton effect occurrence.

7 Parameter Sensitivity Study

The above results clearly show a high sensitivity of ME to MC value and modeling approach. From a mitigation or prevention standpoint, it is also useful to consider ME sensitivity to physical features of the TPJB. This section considers the ME sensitivity to pad rigidity/flexibility and oil supply flowrate. Prior comparisons between simulation and test trends for De Jongh's ME experiments [29] excluded consideration of pad flexibility. Figure 28 shows vibration amplitude at 7000 and 9000 rpm, with and without pad flexibility effects. The ME amplitude growth rate and severity are clearly influenced by pad flexibility at 9000 rpm, as seen in Fig. 28(b). Figure 29(b) shows a similar trend for the peak circumferential temperature difference ΔT, pad flexibility is seen to reduce the severity of the predicted vibrations and ΔT.

Several previous studies [15,18] examined the effect of supply oil flowrate on the ME. However, these studies relied on a conventional MC model of the thermal-flow between pads as discussed in Part I, and which is at least as uncertain as the selected MC. The influence of supply oil flowrate is examined here with the machine learning technique described in Part I. Figures 30 and 31 show that increased supply oil flowrate tends to suppress the severity of the ME in terms of vibration amplitude and circumferential temperature difference (ΔT).

Figure 32 shows temperature contours for the fluid-film domains, for supply oil flowrates of 12 LPM and 21 LPM. The results correspond to a time when the maximum film thickness is located at the pad4 leading-edge, which is the squared region in Fig. 32. The effects of the cool makeup oil are distinctly apparent near the oil inlet (mid-span) and side end, especially for the high supply oil flowrate of 21 LPM. The cooling oil has a deeper penetration toward the shaft surface for the higher supply oil flow case.

Figure 31(b) shows that the higher supply oil flowrates lower the ΔT, which reduces the ME vibration. Injecting cool oil close to the journal surface decreases its temperature and reduces the ME. However, this may be impractical in some applications due to the large increase in bearing oil demand, and its variation with rpm.
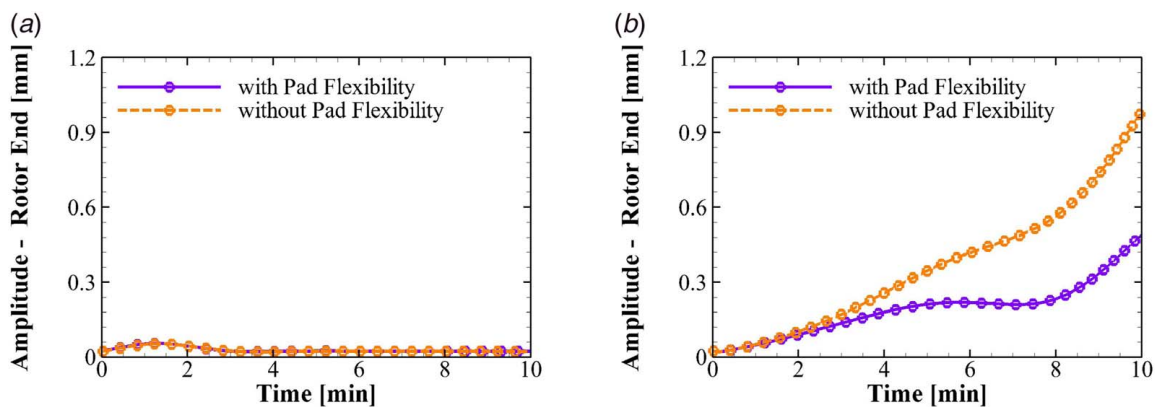

Fig. 28 Peak to peak vibration amplitude at the rotor end versus time, with and without pad flexibility, utilizing the FVM-HBP&MLAMC model: (a) 7000 rpm and (b) 9000 rpm
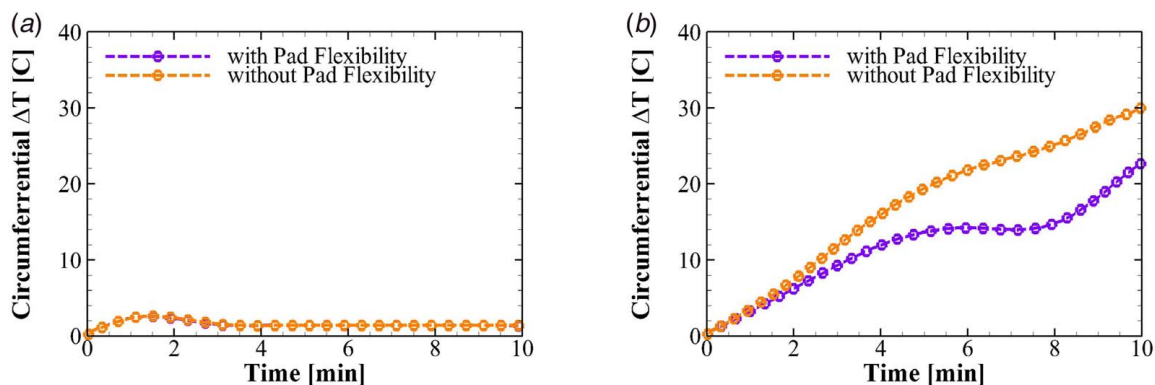

Fig. 29 Circumferential temperature difference (ΔT) versus time, with and without pad flexibility, utilizing the FVM-HBP&MLAMC model: (a) 7000 rpm and (b) 9000 rpm
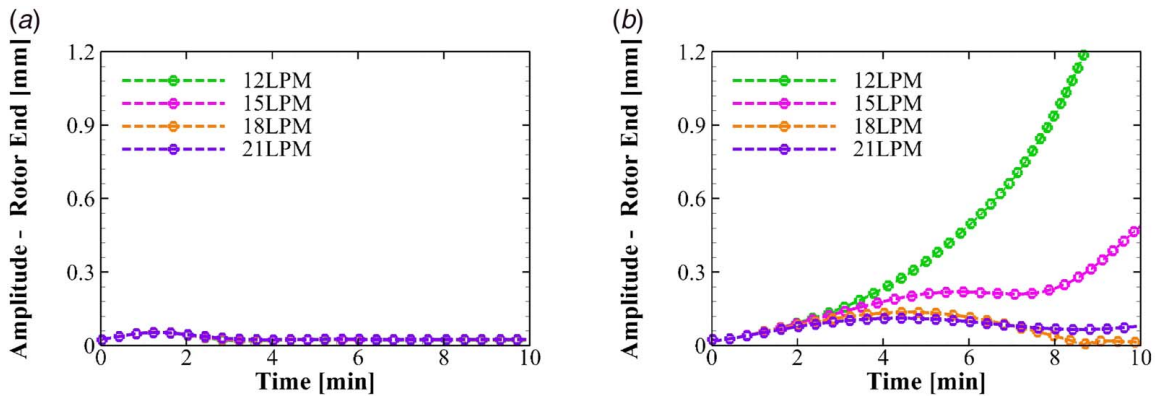
Fig. 30 Peak to peak vibration amplitude at the rotor end versus time, and supply oil flowrate, utilizing the FVM-HBP&MLAMC model: (a) 7000 rpm and (b) 9000 rpm
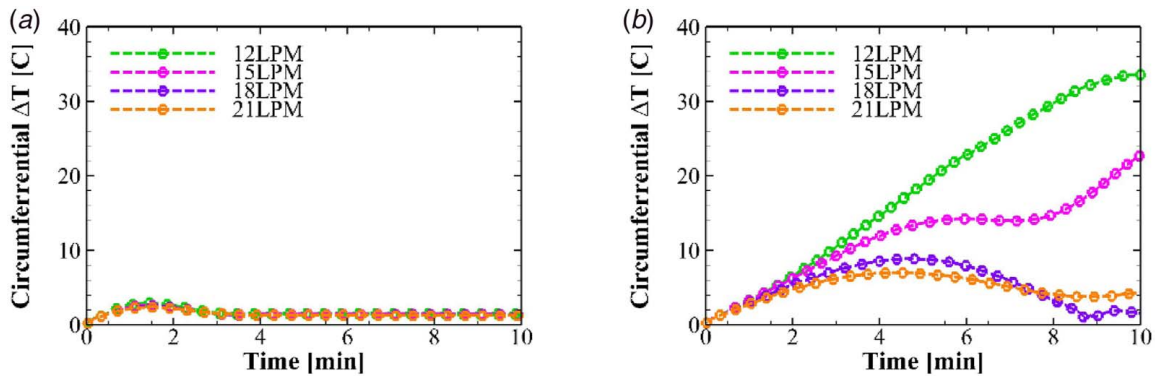

Fig. 31 Circumferential temperature difference (T) versus time, and supply oil flowrate, utilizing the FVM-HBP&MLAMC model: (a) 7000 rpm and (b) 9000 rpm
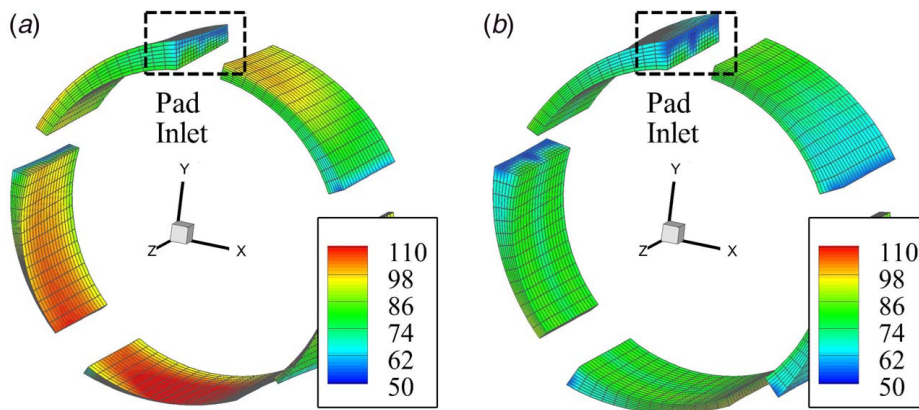

Fig. 32 Fluid-film temperature contours overlaid on deformed film domains at 9000 rpm, for supply oil flowrates (10 min, max. film at pad4 inlet): (a) 12 LPM and (b) 21 LPM

Figure 32(a) shows that the 12 LPM flowrate may have negligible penetration toward the journal surface, and consequently only minor journal cooling effect.

8 Acceleration of Moron Effect Simulation Computational Speed

Accurate simulation of the complex, dynamic, coupled multiphysics ME phenomenon can consume substantial blocks of computer time. This becomes especially acute in an industrial setting where many candidate design configurations must be simulated. Part I

presented a novel, efficient algebraic solver, compatible with numerical time integration. Significant reduction in required computation times was demonstrated for the static equilibrium and dynamic coefficient prediction tasks. The same method is applicable to ME simulation. Figures 33(a) and 33(b) show very large reductions in execution time while using the new computational algorithm in the FVM-based solver.

The elapsed wall clock execution time is for completing the first global time-step (Steps "2, 3, and 4" in Fig. 7). An approximately sevenfold decrease in computation time is achieved for the approximately 30,000 node model utilized in the examples presented. This greatly advances practical implementation of the proposed ME
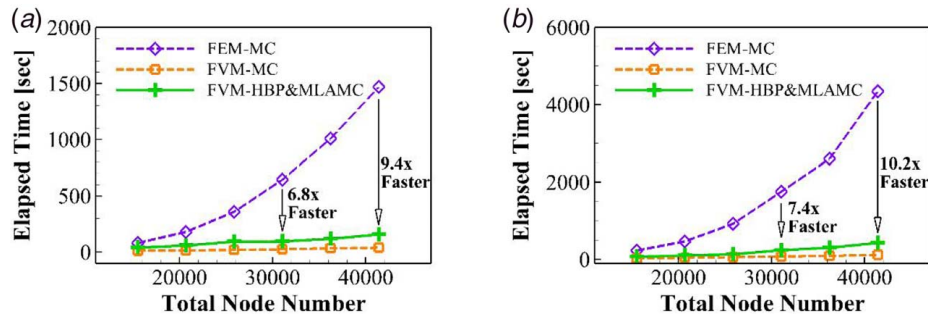
Fig. 33 Elapsed wall clock time for the first global time-step ("2, 3, and 4" in Fig. 7) at (10,000 rpm, 15.142 LPM) in ME simulation: (a) rigid pad and (b) flexible pad

modeling approach for an industrial setting, while even including pad flexibility.

9 Conclusions

This study presented an advanced ME simulation approach, utilizing a quick executing FVM-based, 3D thermo-elasto-hydrodynamic (TEHD) model, combined with a machine learning tool for providing adaptive axial mixing coefficient distributions. Weaknesses of the conventional FEM TEHD TPJB simulation method [12–18] were identified and mitigated by using the new approach. Part I provided an in-depth presentation of the TPJB component modeling methods, including a neural network—machine learning approach for providing axial MC distributions, oil supply flowrates, total supply pressure, and drag torque. Detailed explanations were provided for utilizing the novel FVM-HBP&MLAMC approach for obtaining static equilibrium and dynamic coefficient predictions. Limitations of the conventional FEM-based TEHD TPJB simulation approach were illustrated and remedied by the FVM-HBP&MLAMC approach. These include temperature discontinuities and uniform pad film inlet temperatures, which impede the actual heat flux from the film into the journal and pads. The former resulted from an inability to impose local energy conservation in the film using the FEM approach. The net effect of the FEM-based model limitations were lower journal and pad temperatures, and journal circumferential ΔT.

Uniform pad inlet temperatures result from applying a constant MC over the entire pad film inlet. These MCs are generally guessed and were shown in the paper to have a significant influence on ME effect severity and hot spot and high spot phase angles, and vibration amplitudes. CFD models clearly indicate that MC vary with axial position and vary in time as the parameters that affect the MC vary in time. The practical solution for providing the axial MC as they vary during a ME transient solution was the use of a previously trained ANN machine learning tool.

The need for higher fidelity solutions have been stressed by the authors of Refs. [5,13–18]. This resulted from exposure to a preponderance of field studies reporting on machines experiencing the ME, operating alongside "identical" machines, and operating in "identical" conditions without the ME. This supports the argument that seemingly subtle, insignificant parameter changes can be the decisive factors for the occurrence of the ME. A high fidelity simulation software tool is required in these cases to identify reliable cause and effect mechanisms, to base remedial actions on. The thrust of the present work is to advance the accuracy of ME predictions, in a computationally practical manner. Its accuracy was borne out in the improved consistency between the new method and ME test results [29], as compared with the prior FEM—constant MC approaches.

The proposed FVM-HBP&MLAMC removes the uncertainty from the assumed MC through the HBP model that includes the 3D IBP and 1D OBP models. The HBP model is a combined model with the MLAMC to consider the smaller MC effect near the oil inlet and side end region, and it also takes into account the transient effect due to the non-negligible fluid heat capacity

between pads. This study showed that the conventional MC approach provides reduced shaft temperature prediction due to the neglect of the radial temperature distribution at the fluid-film leading-edge. Additionally, in the case study, the pad flexibility and supply flowrate effects were investigated, and both were shown to reduce ME severity.

The original contribution of the developed model was to develop a much faster and more accurate ME prediction model. The chronic difficulties of the ME simulation require sophisticated modeling techniques and handling a great deal of computational load from the complex dynamic multiphysics system. There is always a trade-off between computation speed and accuracy, but both fast speed and high accuracy are essential for practical ME prediction. In light of the balance of computational speed and accuracy, this research provides a valuable contribution and makes it possible to understand the ME phenomena more clearly.

Conflict of Interest

There are no conflicts of interest.

Data Availability Statement

The authors attest that all data for this study are included in the paper. Data provided by a third party listed in Acknowledgment.

Nomenclature

P = pressure of fluid-film domain, Pa
e_{bw} = thermal imbalance, m
e_{im} = mechanical imbalance, m
m_R = rotor mass, kg
u_{IB} = circumferential velocity of inner BP domain, m/s
v_{IB} = radial velocity of inner BP domain, m/s
w_{IB} = axial velocity of inner BP domain, m/s
w_{OB} = axial velocity of outer BP domain, m/s
x_p = pad total x displacement by dynamic model, m
x_{pvt} = pivot total x displacement in local coordinate, m
x_R = rotor total x displacement by dynamic model, m
x_{tp} = Pad total x displacement by thermal deformation, m
x_{tr} = rotor total x displacement by thermal deformation, m
y_p = pad total y displacement by dynamic model, m
y_R = rotor total y displacement by dynamic model, m
y_{tp} = pad total y displacement by thermal deformation, m
y_{tr} = rotor total y displacement by thermal deformation, m

z_p =	pad total z displacement by dynamic model, m	
z_{tp} =	pad total z displacement by thermal deformation, m	
z_{tr} =	rotor total z displacement by thermal deformation, m	
I_T =	rotor's transverse mass moment of inertia	
T_f =	temperature of fluid-film domain, °C	
T_{IB} =	temperature of inner BP domain, °C	
T_{OB} =	temperature of outer BP domain, °C	
T_P =	temperature of pad domain, °C	
T_R =	temperature of rotor domain, °C	
δ_{tilt} =	pivot total angular displacement, rad	
η =	axial mixing coefficient	

η_{ml} =	machine learning axial mixing coefficient
$\eta_{nn,o}$ =	original neural network axial mixing coefficient
η_o =	original axial mixing coefficient in HBP model
θ_{bw} =	thermal bow, rad
$\theta_{tr,x}$ =	rotor total angular displacement about x axis, rad
$\theta_{tr,y}$ =	rotor total angular displacement about y axis, rad
$\theta_{tr,z}$ =	rotor total angular displacement about z axis, rad
φ_{bw} =	thermal bow phase, rad
φ_{im} =	mechanical imbalance phase, rad
ψ_{bw} =	thermal bow angle phase, rad
ω_R =	rotor spin frequency, rad/s

Appendix

One-Dimensional Finite Element Method Matrix for Two-Dimensional Euler-Bernoulli Beam (Four Degrees-of-Freedom for 1 Node) [33]. Stiffness matrix:

$$\frac{[K_{R,e}]}{(8\times8)} = \frac{E_{R,e}I_{R,e}}{L_{R,e}^3} \begin{bmatrix} 12 & 0 & 0 & 6L_{R,e} & -12 & 0 & 0 & 6L_{R,e} \\ 0 & 12 & -6L_{R,e} & 0 & 0 & -12 & -6L_{R,e} & 0 \\ 0 & -6L_{R,e} & 4L_{R,e}^2 & 0 & 0 & 6L_{R,e} & 2L_{R,e}^2 & 0 \\ 6L_{R,e} & 0 & 0 & 4L_{R,e}^2 & -6L_{R,e} & 0 & 0 & 2L_{R,e}^2 \\ -12 & 0 & 0 & -6L_{R,e} & 12 & 0 & 0 & -6L_{R,e} \\ 0 & -12 & 6L_{R,e} & 0 & 0 & 12 & 6L_{R,e} & 0 \\ 0 & -6L_{R,e} & 2L_{R,e}^2 & 0 & 0 & 6L_{R,e} & 4L_{R,e}^2 & 0 \\ 12 & 0 & 0 & 2L_{R,e}^2 & -6L_{R,e} & 0 & 0 & 4L_{R,e}^2 \end{bmatrix}$$

Mass matrix:

$$\frac{[M_{R,i}]}{(4\times4)} = \begin{bmatrix} m_{R,i} & 0 & 0 & 0 \\ 0 & m_{R,i} & 0 & 0 \\ 0 & 0 & I_{T,i} & 0 \\ 0 & 0 & 0 & I_{T,i} \end{bmatrix}$$

Gyroscopic matrix:

$$\frac{[C_{gs,i}]}{(4\times4)} = \begin{bmatrix} 0 & 0 & 0 & 0 \\ 0 & 0 & 0 & -\omega_R I_{P,i} \\ 0 & 0 & 0 & 0 \\ 0 & 0 & \omega_R I_{P,i} & 0 \end{bmatrix}$$

$m_{R,i}$: rotor mass at node i, $I_{R,e}$: area moment of inertia, $I_{T,i}$: rotor's transverse mass moment of inertia at node i, $I_{P,i}$: polar mass moment of inertia, ω_R: rotor spin frequency, $L_{R,e}$: element length, $E_{R,e}$: element Young's modulus.

References

[1] Morton, P. G., 1975, "Some Aspects of Thermal Instability in Generators," G.E.C. Internal Report No. S/W40 u183.

[2] Hesseborn, B., 1978, "Measurements of Temperature Unsymmetries in Bearing Journal Due to Vibration," Internal Report ABB Stal.

[3] De Jongh, F., 2008, "The Synchronous Rotor Instability Phenomenon—Morton Effect," 37th Turbomachinery Symposium, Houston, TX, Sept. 8–11, pp. 159–167.

[4] Panara, D., Panconi, S., and Griffini, D., 2015, "Numerical Prediction and Experimental Validation of Rotor Thermal Instability," 44th Turbomachinery Symposium, Houston, TX, Sept. 14–17.

[5] Tong, X., Palazzolo, A., and Suh, J., 2017, "A Review of the Rotordynamic Thermally Induced Synchronous Instability (Morton) Effect," ASME Appl. Mech. Rev., 69(6), p. 060801.

[6] Keogh, P., and Morton, P., 1993, "Journal Bearing Differential Heating Evaluation With Influence on Rotor Dynamic Behaviour," Proc. R. Soc. London, Ser. A, 441(1913), pp. 527–548.

[7] Keogh, P., and Morton, P., 1994, "The Dynamic Nature of Rotor Thermal Bending Due to Unsteady Lubricant Shearing Within a Bearing," Proc. R. Soc. London, Ser. A, 445(1924), pp. 273–290.

[8] Gomiciaga, R., and Keogh, P., 1999, "Orbit Induced Journal Temperature Variation in Hydrodynamic Bearings," ASME J. Tribol., 121(1), pp. 77–84.

[9] Balbahadur, A. C., and Kirk, R., 2004, "Part I—Theoretical Model for a Synchronous Thermal Instability Operating in Overhung Rotors," Int. J. Rotating Mach., 10(6), pp. 469–475.

[10] Balbahadur, A. C., and Kirk, R., 2004, "Part II—Case Studies for a Synchronous Thermal Instability Operating in Overhung Rotors," Int. J. Rotating Mach, 10(6), pp. 477–487.

[11] Murphy, B., and Lorenz, J., 2010, "Simplified Morton Effect Analysis for Synchronous Spiral Instability," ASME J. Vib. Acoust., 132(5), p. 051008.

[12] Childs, D., and Saha, R., 2012, "A New, Iterative, Synchronous-Response Algorithm for Analyzing the Morton Effect," ASME J. Eng. Gas Turbines Power, 134(7), p. 072501.

[13] Lee, J., and Palazzolo, A., 2012, "Morton Effect Cyclic Vibration Amplitude Determination for Tilt Pad Bearing Supported Machinery," ASME J. Tribol., 135(1), p. 011701.

[14] Suh, J., and Palazzolo, A., 2014, "Three-Dimensional Thermohydrodynamic Morton Effect Simulation—Part I: Theoretical Model," ASME J. Tribol., 136(3), p. 031706.

[15] Suh, J., and Palazzolo, A., 2014, "Three-Dimensional Thermohydrodynamic Morton Effect Analysis—Part II: Parametric Studies," ASME J. Tribol., 136(3), p. 031707.

[16] Tong, X., Palazzolo, A., and Suh, J., 2016, "Rotordynamic Morton Effect Simulation With Transient, Thermal Shaft Bow," ASME J. Tribol., **138**(3), p. 031705.

[17] Tong, X., and Palazzolo, A., 2017, "Double Overhung Disk and Parameter Effect on Rotordynamic Synchronous Instability—Morton Effect—Part I: Theory and Modeling Approach," ASME J. Tribol., **139**(1), p. 011705.

[18] Tong, X., and Palazzolo, A., 2017, "Double Overhung Disk and Parameter Effect on Rotordynamic Synchronous Instability—Morton Effect—Part II: Occurrence and Prevention," ASME J. Tribol., **139**(1), p. 011706.

[19] Monmousseau, P., and Fillon, M., 2000, "Transient Thermoelastohydrodynamic Analysis for Safe Operating Conditions of a Tilting-Pad Journal Bearing During Start-up," Tribol. Int., **33**(2), pp. 225–231.

[20] Fillon, M., Bligoud, J. C., and Frene, J., 1992, "Experimental Study of Tilting-Pad Journal Bearings—Comparison With Theoretical Thermoelastohydrodynamic Results," ASME J. Tribol, **114**(3), pp. 579–587.

[21] Fillon, M., and Bouyer, J., "Thermohydrodynamic Analysis of a Worn Plain Journal Bearing," Tribol. Int., **37**(2), pp. 129–136.

[22] Haugaard, A. M., and Santos, I. F., 2010, "Multi-Orifice Active Tilting-Pad Journal Bearings—Harnessing of Synergetic Coupling Effects," Tribol. Int., **43**(8), pp. 1374–1391.

[23] Brito, F. P., Miranda, A. S., Claro, J. C. P., and Fillon, M., 2012, "Experimental Comparison of the Performance of a Journal Bearing With a Single and a Twin Axial Groove Configuration," Tribol. Int., **54**, pp. 1–8.

[24] Lin, Q., Wei, Z., Wang, N., and Chen, W., 2013, "Analysis on the Lubrication Performances of Journal Bearing System Using Computational Fluid Dynamics and Fluid-Structure Interaction Considering Thermal Influence and Cavitation," Tribol. Int, **64**, pp. 8–15.

[25] Brito, F. P., Miranda, A. S., Claro, J. C. P., Teixeira, J. C., Costa, L., and Fillon, M., 2014, "The Role of Lubricant Feeding Conditions on the Performance Improvement and Friction Reduction of Journal Bearings," Tribol. Int., **72**, pp. 65–82.

[26] Yang, J., and Palazzolo, A., 2019, "Three-Dimensional Thermo-Elasto-Hydrodynamic CFD Model of a Tilting Pad Journal Bearing-Part I: Static Response," ASME J. Tribol., **141**(6), p. 061702.

[27] Yang, J., and Palazzolo, A., 2020, "Computational Fluid Dynamics Based Machine Learning Mixing Prediction for Tilt Pad Journal Bearing TEHD Modeling——Part I: Model Validation and Improvements," ASME J. Tribol., **143**(1), p. 011801.

[28] Yang, J., and Palazzolo, A., 2020, "Computational Fluid Dynamics Based Machine Learning Mixing Prediction for Tilt Pad Journal Bearing TEHD——Part II: Artificial Neural Network Machine Learning," ASME J. Tribol., **143**(1), p. 011802.

[29] De Jongh, F., and Van Der Hoeven, P., 1998, "Application of a Heat Barrier Sleeve to Prevent Synchronous Rotor Instability," 27th Turbomachinery Symposium, Houston, TX, Sept. 20–24, pp. 17–26.

[30] Oh, J., Palazzolo, A., and Hu, L., 2020, "Stability of Non-Axisymmetric Rotor and Bearing Systems Modeled With Three-Dimensional-Solid Finite Elements," ASME J. Vib. Acoust., **142**(1), p. 011010.

[31] Hagemann, T., Zeh, C., and Schwarze, H., 2019, "Heat Convection Coefficients of a Tilting-Pad Journal Bearing With Directed Lubrication," Tribol. Int., **136**, pp. 114–126.

[32] Tong, X., and Palazzolo, A., 2018, "Tilting Pad Gas Bearing Induced Thermal Bow-Rotor Instability," Tribol. Int., **121**, pp. 269–279.

[33] Palazzolo, A., 2016, *Vibration Theory and Applications With Finite Elements and Active Vibration Control*, Wiley, New York, Chichester, UK.